# Polarity reversal by centrosome repositioning primes cell scattering during epithelial-to-mesenchymal transition

# Polarity Reversal by Centrosome Repositioning Primes Cell Scattering during Epithelial to Mesenchymal Transition

Mithila Burute [1,2,3], Magali Prioux [2], Guillaume Blin [4], Sandrine Truchet [5], Gaëlle Letort [2], Qingzong Tseng [2], Thomas Bessy [1], Sally Lowell[4], Joanne Young[3], Odile Filhol-Cochet [6], Manuel Théry [1,2*]

[1] CytoMorpho Lab, A2T, UMRS1160, Institut Universitaire d'Hématologie, Hôpital Saint Louis, INSERM/AP-HP/Université Paris Diderot, 1 Avenue Claude Vellefaux, 75010 Paris, France.
[2] CytoMorpho Lab, LPCV, UMR5168, Biosciences & Biotechnology Institute of Grenoble, CEA/INRA/CNRS/Université Grenoble-Alpes, 17 rue des Martyrs, 38054 Grenoble, France.
[3] CYTOO SA, 7 Parvis Louis Néel, 38040 Grenoble, France.
[4] MRC Centre for Regenerative Medicine, Institute for Stem Cell Research, School of Biological Sciences, University of Edinburgh, 5 Little France Drive, EH16 4UU Edinburgh, United Kingdom.
[5] GABI, INRA/AgroParisTech/Université Paris-Saclay, Domaine de Vilvert, 78352 Jouy-en-Josas, France.
6 Laboratoire de Biologie du Cancer et de l'Infection, UMRS1036, Biosciences & Biotechnology Institute of Grenoble, CEA/INSERM/Université Grenoble-Alpes, 17 rue des Martyrs, 38054 Grenoble, France.

*Correspondence: manuel.thery@cea.fr

## Summary

During epithelial to mesenchymal transition (EMT), cells lining the tissue periphery break up their cohesion to migrate within the tissue. This dramatic reorganization involves a poorly characterized reorientation of the apico-basal polarity of static epithelial cells into the front-rear polarity of migrating mesenchymal cells. To investigate the spatial coordination of intracellular reorganization with morphological changes, we monitored centrosome positioning during EMT in vivo, in developing mouse embryos and mammary gland, and in vitro, in cultured 3D cell aggregates and micro-patterned cell doublets. In all conditions, centrosomes moved from their off-centered position next to intercellular junctions toward extra-cellular matrix adhesions on the opposite side of the nucleus, resulting in an effective internal polarity reversal. This move appeared supported by controlled microtubule network disassembly. Sequential release of cell confinement using dynamic micropatterns, and modulation of microtubule dynamics, confirmed that centrosome repositioning was responsible for further cell disengagement and scattering.

## Introduction

Epithelium provides a selective barrier for controlled directional transport in duct containing organs such as airway, intestinal track or secretory tubule glands. Cells of epithelial origins are internalized at specific developmental stages to subsequently form internal tissues (Acloque et al., 2009). As they do so, some epithelial cells convert into mesenchymal cells, which migrate into and populate the underlying interstitial tissues. This topological tissue remodeling, during which peripheral cells become internal cells, is accompanied by dramatic intra-cellular reorganization (Lamouille et al., 2014). Epithelial cells disassemble the tight junctions they formed with their neighbors and that were ensuring the selective permeability. As they move inside, they lose the contact-free edge they had toward the outer medium and get fully surrounded by cells and extra-cellular matrix (Acloque et al., 2009). Their secretory and endocytic functions, which were directed by the presence of this contact-free interface get redistributed toward adhesive edges. Therefore the epithelial-to-mesenchymal transition (EMT) not only involves reorganization of cell position and acquisition of a migratory phenotype but also implies a reorientation of cell function and polarity (Godde et al., 2010; Huang et al., 2012).

Cell polarity is an intrinsic bias in internal cell organization which is spatially adapted to extra-cellular cues and which direct cell functions (Bornens, 2008). In epithelia, intercellular junctions form a diffusion barrier between distinct plasma membrane domains and thus define the apical pole, toward the outer medium, and the basal pole, toward the extra-cellular matrix (ECM) that cells are attached to (Rodriguez-Boulan and Macara, 2014). The spatial segregation of cell-matrix adhesion and intercellular junctions physically separate the signaling and anchoring proteins they are associated with (Burute and Thery, 2012). The centrosome is off-centered toward the actin-rich apical pole (Hebert et al., 2012) and microtubule orientation along the apico-basal axis directs intra-cellular trafficking (Akhtar and Streuli, 2013). Together, the segregation of the two types of adhesions and the orientation of the microtubule network defines the apico-basal orientation of epithelial cell polarity from ECM toward the contact free edge. In mesenchymal cells, intercellular junctions are much weaker and do not define membrane domains as in epithelial cells. Instead, it is the cell migration machinery that directs cell polarity (Etienne-Manneville, 2013). Here also, mutual exclusion of signaling pathways segregate actin network polymerization at the advancing cell edge and actin contraction at the retracting edge and thereby define the mesenchymal front-rear polarity axis. Centrosome positioning toward the cell front and the associated asymmetric microtubule network organization is pivotal for the establishment and maintenance of the front-rear polarity axis of migrating cells (Etienne-Manneville, 2013; Luxton and Gundersen, 2011). Thus, during EMT the apico-basal polarity axis is converted into a front-rear axis (Godde et al., 2010; Nelson, 2009; Xu et al., 2009). The mechanism involved in the remodeling of cell internal polarity during this conversion has not yet been specifically addressed.

Simple geometrical considerations suggest that during EMT the epithelial polarity toward the contact-free edge is literally inverted toward the underlying

basement membrane that mesenchymal cells digest as they move inward (Figure S1). Several examples of such polarity reversals have been observed within simplified epithelia in vitro, in response to conditions that are close to the changes that occur during EMT. Thus, modifying the composition of the extra-cellular matrix surrounding epithelial cyst, or modulation of integrins activation state, can induce the relocalization of polarity surface markers from the outside surface to the internal lumen and vice versa (Akhtar and Streuli, 2013; Nitsch and Wollman, 1980; Ojakian and Schwimmer, 1994; Rodriguez-Fraticelli et al., 2012; Wang et al., 1990; Yu et al., 2005). While the characterization of the mechanism supporting the inversion of surface markers and membrane protrusions has been addressed (Bryant et al., 2014; Scarpa et al., 2015), the reorganization of intracellular organization has not yet been studied. Interestingly, analyses of intermediate stages of developing chick auditory system and neural network, as well as observations of branching kidney tubules and inversion of thyroid follicles in culture have suggested the existence of concerted repositioning of internal organelles such as nucleus, Golgi apparatus, lysosomes and centrosome (Carney and Couve, 1989; Das and Storey, 2014; Nitsch and Wollman, 1980; Pollack et al., 1998; Yu et al., 2003). The synchrony between centrosome repositioning and epithelial cell migration within the underlying mesenchyme led to the hypothesis that internal polarity reversal is instrumental in the initiation of cell migration (Carney and Couve, 1989).

This hypothesis is supported by the observation of nucleus-centrosome axis orientation toward ECM rather than intercellular junctions in cells that are prompt in scattering (Desai et al., 2009). However epithelial transition to cell migration can occur without Golgi apparatus and centrosome repositioning (Anstrom and Raff, 1988; Revenu et al., 2014). Indeed, all cells don't migrate with the centrosome in front of the nucleus (Higginbotham and Gleeson, 2007; Luxton and Gundersen, 2011; Pouthas et al., 2008; Tang and Marshall, 2012). Centrosome locates behind the nucleus of migrating lymphocytes (Takesono et al., 2010) and its position in neutrophils (Yoo et al., 2012) and migrating fibroblasts (Yvon et al., 2002) is debated. Some of the observed differences certainly come from the strong effect of cell microenvironment. Indeed, subtle variations of microenvironment geometry can reverse centrosome position in a given migrating cell type (Pouthas et al., 2008), making difficult to compare in vitro and in vivo conditions. Furthermore the mixed contributions of cell-cell contact, the process of migration itself and the multiple mechanisms regulating, together or separately, the position of nucleus and of centrosome add to the confusion (Luxton and Gundersen, 2011; Tang and Marshall, 2012). In the end, whether centrosome position is a cause or a consequence of cell migration could not be clarified. New methodological approaches appeared required to test whether internal polarity is actually reversed during EMT and whether it promotes or follows the cell migration process.

Here we use in-vitro models of mammary gland development (Debnath et al., 2003) and kidney tubulogenesis (Pollack et al., 1998) to study cell polarity during epithelial morphogenesis. In order to distinguish the effect of cell neighbors, cell migration, cell spreading and adhesion remodeling on cell polarization, we use micropatterns to control the shape and position of cells forming doublets. We show

that nucleus-centrosome axis reorientation occurs in the few hours following mammary gland cells stimulation with transforming growth factor beta (TGF-β) and kidney cells stimulation with either TGF-β or hepatocyte growth factor (HGF). Centrosome repositioning at the cell center appeared driven by a partial disassembly of the microtubule network and the release of Partitioning defective protein Par3 from intercellular junctions. Finally, we show that polarity reversal by centrosome repositioning occurs prior to cell scattering and was necessary for cell dissociation during EMT.

## Results

### Polarity reversal during EMT in mouse development

Several key developmental stages involve EMT and thus could display the polarity reversal we hypothesize. The first EMT event occurs at gastrulation, 5-6 days post fertilization. The primitive streak forms at the future posterior end of the embryo wherein a subset of epiblast cells differentiate into primary mesenchyme and ingress between the epiblast and endoderm layer (Acloque et al., 2009; Tam and Behringer, 1997). Epiblast cells are marked by expression of nuclear T-Brachyury along with breakdown of Collagen IV (Figure 1A). Using γ-tubulin as a marker for centrosome, we investigated polarity of cell populations destined for different cell fates. The centrosome in epiblast cells was localized close to the amniotic cavity, resulting in a nucleus-centrosome axis oriented toward the cavity. The epiblast cells undergoing EMT showed higher T-Brachyury expression and were positioned farther from the cavity. In these cells, centrosomes appeared relocated away from the cavity and the nucleus-centrosome axis pointed toward the endoderm layer (Figure 1B, C). This supported our hypothesis that upon the onset of EMT, when epiblast cells move inward to form the primitive streak, the nucleus-centrosome axis gets inverted.

Later, at puberty, the ductal network within the mouse mammary gland expands by invading the surrounding fat pad. At this stage, specialized structures called terminal end buds appear at the end of the primary ducts (Hinck and Silberstein, 2005). Cell rearrangement and the collective migration of cells out of the bud is based on partial EMT (as the cells did not transit up to individual migration) (Ewald et al., 2008; Godde et al., 2010). Cell polarity axis orientation was inferred from the orientation of the Golgi apparatus with respect to the nucleus. In luminal cells, the Golgi apparatus was positioned toward the duct (Figure 1D) as in the case of lactating acini (Akhtar and Streuli, 2013). Interestingly, a few cells at the tip of the growing terminal end buds showed complete inversion of the nucleus-Golgi axis (Figure 1D and Movie S1). Other cells near the tip displayed a mispositioned Golgi apparatus suggestive of intermediate stages of polarity reversal (Figure 1D).

We thus found indications of nucleus-centrosome axis inversion at two distinct stages of mouse development, supporting our working hypothesis of polarity reversal occurring during EMT. Investigating the mechanics of polarity inversion in vivo at single cell resolution remains technically challenging. In order to obtain further insights into this process we used simpler and more accessible working systems to study the induction and consequences of those polarity reversals where parameters of interest could be better controlled.

### Polarity reversal in 3D mammary gland cell culture

Self-organized mammary acini in 3D gels recapitulate numerous features of native tissue, including epithelial cell polarization (Debnath et al., 2003) and constitute a robust system amenable to induction of morphogenesis by the addition of growth factors (Debnath et al., 2003; Montesano et al., 2007; Seton-Rogers et al., 2004). We used MCF10A 3D cultures as a model of mammary gland acini to investigate polarity

changes that may occur upon induction of EMT by TGF-β (Xu et al., 2009; Zhang et al., 2014) (Figure S2A-C). After seven days culture in 3D gels of laminin-rich basement membrane (commercialized as Matrigel), MCF10A show acini-like structures with enriched apical actin indicating the site of a future lumen (Figure 1E). Nontreated cysts showed a regular arrangement of nuclei in a single layer and were placed equidistant from the acinus center (Figure 1E). This regular geometric organization was lost in cysts treated with TGF-β1 (5 ng/ml) for 5 days. The severe disorganization of cell arrangement in cysts was also associated with misorientation of the polarity axes (Figure 1E, F). We found a similar disorganization of acini assembled from MDCK cells of kidney origin upon treatment with HGF (Figure S2D-G). Thus, cell mispositioning and polarity axes disorientation are closely connected in these 3D architectures. This complex interplay between cell shape, position and polarity raised a few central questions that are difficult to address in 3D culture systems. In particular, polarity misorientation could result from defective internal polarization mechanism or from a correct polarization in a perturbed context due to mispositioning of neighboring cells. Furthermore, cell migration is known to actively regulate both epithelial (Wang et al., 2013) and mesenchymal (Luxton and Gundersen, 2011) cell polarities, suggesting that cell motility could also actively direct polarity reorientation in these 3D cysts.

**Polarity reversal in micropatterned cells**

It appeared necessary to dissect the role of cell polarization, cell positioning and cell motion in tissue reorganization during EMT. This prompted us to work on a simpler but more controlled cell culture model, which can still recapitulate important aspects of morphogenesis (Théry, 2010). We first aimed at eliminating the variable effect due to the presence of multiple neighbors and their movement by adapting a minimal tissue model of 2 cells confined on micropattern geometry. To prevent the possible effect of cell movement on polarity reversal we looked for micropattern geometries that could block cell migration. Restricting micropattern size is not sufficient to prevent cell movement because cells can exchange their positions and rotate within the micropatterned area (Tseng et al., 2012). Square-shaped micropatterns could not prevent the rotation of normal epithelial cells and were even less able to constrain that of TGF-β -induced mesenchymal cells (Figure 2A, left). Bowtie-shaped micropatterns stabilized the position of epithelial cells but could not prevent mesenchymal cell motion (Figure 2A, middle). H-shaped micropattern could block both epithelial (Tseng et al., 2012) and mesenchymal cell motion, placing them in similar and thus comparable conditions (Figure 2A, right). Hence H-shaped micropatterns were used in further experiments to compare epithelial and mesenchymal cell polarity.

Single MCF10A or MDCK cells were plated on H-shaped micropatterns and fixed 24 hour later to give them enough time to divide once and form daughter cell doublets (Figure 2B). Nucleus-centrosome vector orientations were measured with respect to the nucleus-nucleus axis pointing toward the intercellular junction (Figure 2C). Nucleus-centrosome distances were normalized with respect to nucleus size (Figure 2C). Thus, positive coordinates corresponded to nucleus-centrosome axes pointing

toward adjacent cells and large values to highly eccentric centrosome positions. Both epithelial MCF10A (cultured in defined medium) and MDCK cells (cultured in classical growth medium with serum) displayed marked polarization toward the intercellular junction (Figure 2D). Strikingly, MCF10A cells pretreated with TGF-β for 5 days and MDCK cells pretreated with HGF for 3 days both displayed the opposite polarity orientation (Figure 2D), although contacting cells were still interacting and pulling on each others (Figure S3A, B). This polarity reversal was also quantified by measuring the centrosome X coordinate along the nucleus-nucleus axis, hereafter referred to as the cell polarity index toward intercellular junction. The coordinate sign change attests to the centrosome repositioning from the nucleus side oriented toward the intercellular junction to the side oriented toward extra-cellular matrix adhesions (Figure 2E). Interestingly, in MCF10A treated with TGF-β, this polarity reversal was due to both centrosomes moving away from the junction to the cell center and nuclei moving away from cell-matrix adhesions toward intercellular junction (Figure 2E, Figure S3C). By contrast, in MDCK, nuclei positioning was not affected by HGF treatment, and centrosome repositioning alone contributed to polarity reversal (Figure 2E).

**Matrix stiffness promotes polarity reversal**

We further investigated centrosome repositioning in other classical models of EMT. NMuMG and EpH4 are luminal mammary cells that are known to be highly sensitive to EMT induction (Lamouille and Derynck, 2007; Montesano et al., 2007) (Figure S2H, I). To our surprise, when plated on micropatterns, both cell types were polarized toward cell matrix adhesion (mesenchyme-like polarity) and not toward inter-cellular junction. Since TGF-β was absent from the growth factor-defined serum-free culture medium, we reasoned that EMT might have been induced by the cell culture substrate. Indeed, matrix stiffness is a potent EMT inducer (Markowski et al., 2012; Wei et al., 2015). Cells were thus plated on micropatterned poly-acrylamide gels of controlled stiffness (Vignaud et al., 2014). On such soft substrates, cell doublets spread to a lesser extent and adopted a more compact geometry. When cultured on 10kPa gels, EpH4 displayed a typical epithelial polarity with the nucleus-centrosome axis oriented toward intercellular junctions, opposite to their polarization on glass (Figure 3A). Stiffness had to be further reduced to 1 kPa for NMuMG to recover a typical epithelial-like polarity (Figure 3B). These results show that matrix stiffness is sufficient to induce polarity reversal in the absence of TGF-β and thereby predispose epithelial cells to a mesenchyme transition. They also revealed that polarity reversal is quite reactive to EMT factors and that it can be easily induced in sensitive epithelial cells in response to mechanical and/or biochemical stimulations.

**Polarity reversal is an early feature of EMT.**

Cell sensitivity to EMT inducers prompted us to evaluate the timing of centrosome repositioning during the EMT process. TGF-β treatment is known to take several days to induce a full EMT but the very first changes appear a few hours after TGF-β addition (D'Souza et al., 2014). Cells were first plated on micropatterns and then treated with TGF-β for increasing periods of time. In MCF10A, centrosome repositioned in less than 24 hours (Figure 2F). In MDCK, TGF-β effects were detectable

after 4 hours of treatment and polarity was reversed after 8 hours only. HGF effects on MDCK were even faster; centrosome repositioned almost immediately and inversion was completed within 4 hours (Figure 2F). These data imply that centrosome repositioning is an early sign of EMT concomitant with the first changes in protein expression following TGF-β addition (D'Souza et al., 2014). All further experiments were performed by 5 day treatment of TGF-β to MCF10A and 3 day treatment of HGF to MDCK unless specifically mentioned.

**Microtubule network remodeling accompany centrosome re-centering**

We further investigated the mechanism by which centrosome leaves its off-centered position next intercellular junctions to position at the cell center during EMT. Since centrosome positioning mostly depends on the microtubule network (Mimori-Kiyosue, 2011; Tang and Marshall, 2012), we compared microtubule network architectures before and after induction of EMT to gain further insight in the mechanism supporting centrosome repositioning. TGF-β treatment induced a drop in the total amount of microtubules (Figure 4A). Interestingly, the portion of TGF-β treated cells, which retained their centrosome position toward intercellular junction, like the control cells, harbored more microtubules (Figure 4A). These changes could be quantified by the diminution of polymerized α–tubulin intensity (Figure 4A) as well as the reduction in the number of EB1 comets (Figure 4B). Those differences could be explained by a reduction of centrosomal microtubules, as suggested by the reduction in γ-tubulin intensity (Figure 4B) and the number of EB1 comets at the centrosome (Figure 4B). These observations suggest that the high amount of microtubules may be responsible for centrosome off-centering in epithelial cells and its decrease would promote its recentring in mesenchymal cells. We tested this new hypothesis by performing numerical simulations with Cytosim (Nedelec and Foethke, 2007) in which the number of microtubules was modulated. Asters were constrained to grow in a confined space similar to the cell shape obtained on square micropatterns. Cytoplasmic dyneins were scattered throughout the cytoplasm so that their minus-end directed motion could promote aster centering by exerting pulling forces on microtubules (Wu et al., 2011). Microtubules were allowed to glide along and to push on cell edges as they grow. Interestingly, at low microtubule numbers (10-100), asters moved and stabilized at the cell center whereas with higher numbers of microtubules (200-350), the pushing forces exceeded the centering force and moved the centrosome off-center, toward the cell edge (Figure 4C, movie S2). Measuring centrosome final position in relation to the number of microtubules confirmed this observation (Figure 4D). Importantly, this behavior was quite robust and did not depend on centrosome initial position (Figure 4E). We further experimentally tested whether increasing microtubule number in TGF-β treated cells could restore centrosome off-centering close to the intercellular junction. To do so, we knocked down microtubule destabilizing protein Op18/stathmin in TGF-β treated cells (Belmont and Mitchison, 1996). Forty-eight hour post stathmin siRNA treatment; we observed clear restoration of centrosome position of EMT induced cells along with increase in the microtubule number (Figure 4F). The position of nucleus-golgi axis was also restored in the acini transfected with stathmin siRNA (Figure 4G). In addition, 5

hour of taxol treatment to TGF-β treated cells increased the microtubule bundles and also restored the off-centered centrosome position like that of non-treated cells (Figure 4H). These results suggest that the amount of polymerized tubulin was responsible for the transition from an off-centered microtubule network in epithelial cells to a centered conformation in mesenchymal cells.

**Par3 regulates centrosome repositioning during EMT**

In our numerical simulations, no external bias was added to direct centrosome off-centering toward a specific cell edge. Partitioning defective proteins (PAR) polarity complexes Par3/Par6/aPKC, β-catenin and dyneins along intercellular junctions could actively bias this process by stabilizing and pulling on microtubules (Harris and Peifer, 2007; Ligon et al., 2001; Schmoranzer et al., 2009). To test whether such a mechanism was active in our conditions, we first quantified microtubule abundance along intercellular junction. Both tubulin intensity and EB1 comets were reduced along the junction of TGF-β treated cells (Figure 5A). Furthermore population of stabilized microtubules labeled by acetylated tubulin was significantly reduced at the cell-cell junction (Figure 5B). These results argued in favor of a mechanism of centrosome off-centering toward intercellular junctions in epithelial cells by local microtubule stabilization.

Intercellular junctions remained but were altered in TGF-β treated cells (Figure S3). Disappearance of Par3 from intercellular junctions could be involved in centrosome release since they it has been shown to regulate centrosome positioning in a wide range of cell types (Feldman and Priess, 2012; Oliaro et al., 2010; Schmoranzer et al., 2009; Solecki et al., 2009; St Johnston and Sanson, 2011). Par3 is notably involved in centrosome translocation from central to apical positioning during mesenchyme-to-epithelium transitions during neurulation (Hong et al., 2010). As intuited, Par3 localization along intercellular junction was drastically reduced after 5-day treatment of TGF-β (Figure 5C). Interestingly the junction density of Par3 along intercellular junctions appeared correlated to centrosome positioning: the higher the concentration of Par3 the closer the centrosome (Figure 5C). Inhibition of signaling downstream of TGF-β type I receptor by SB431542 (Inman et al., 2002) restored Par3 levels and centrosome off-centering toward intercellular junction (Figure 5C, D). Furthermore down-regulation of Par3 levels by Pard3 siRNA in untreated MCF10A cells increased the inter-centrosome distance (Figure 5E), while Par3b overexpression in TGF-β (3 day) treated cells restored centrosome position toward intercellular junction (Figure 5E-F), further confirming Par3 implication in the regulation of centrosome repositioning during EMT.

**Centrosome repositioning promotes cell scattering**

Centrosome repositioning in immobilized cells on H-shaped micropattern showed that it was not a consequence of cell motion. Nucleus-centrosome reorientation toward cell-matrix adhesion even suggested cells were predisposed to separate. But whether centrosome repositioning could actually trigger cell scattering

remained to be tested. We first used micropatterned tracks on which cells were free to separate from each other. In three distinct epithelial cell lines, untreated cells stayed in contact whereas the majority of TGF-β treated cells separated after division (Figure 6A, Movie S3). Similarly, single end point assay based on inter-nuclear distance in cell doublets revealed higher cell scattering in TGF-β or HGF treated cells (Figure 6B). Importantly, TGF-β or HGF-treated-cells that were still in contact showed twice more conformations with reversed centrosome position compared to control cells, suggesting that centrosome repositioning preceded cell scattering (Figure 6C). We tested the positive effect of microtubule disassembly in cell scattering upon EMT induction by adding Taxol to TGF-β treated cells. Five hours of taxol treatment did reduce cell scattering (Figure 6D). Par3 overexpression also had a modest reduction effect on cell scattering (Figure 6D). Interestingly, and consistent with our previous observations on centrosome repositioning, high stathmin levels have been shown to stimulate cell migration during EMT and cancer metastasis (Li et al., 2011; Lu et al., 2014). Here, we observed 30% drop in cell scattering upon stathmin knockdown (Figure 6D). As stathmin is activated by a MEK/ERK-dependent phosphorylation (Filbert et al., 2012), we inhibited the MEK pathway in EMT induced cells with UO126 and also observed a strong reduction of cell scattering (Figure 6D). These effects were likely due to centrosome repositioning rather than increased microtubule stability that has been shown to promote rather than impair individual cell migration (Zhang et al., 2011). Taken together these observations support the view that EMT-induced cell separation is intimately coupled to centrosome re-centering via stathmin-dependent microtubule disassembly.

To directly test whether centrosome repositioning was actually causing cell scattering we looked for a way to induce it, or not, before cells had the opportunity to move away from each other. We decided to use dynamic micropatterning to release confined cells with pre-established epithelial or inverted polarities.

Dynamic micropatterning relies on the use of click chemistry to graft RGD peptides to the PEG chains preventing cell adhesion around micropatterns (van Dongen et al., 2013). The mild conditions of the azide-alkyne cycloaddition offer the possibility to graft a RGD-alkyne compound to a PEG-azide chain in the presence of living cells (Figure 7A). Thus, micropatterned cells can start migrating out of the micropattern upon addition and grafting of RGD groups to the PEG chains.

We first confirmed the expected outcomes of EMT induction, i.e. that most MCF10A epithelial cells remain in contact with each other while TGF-β treated cells tend to separate within 4 hour after cell release by addition of RGD (Figure 7B). We further took advantage that not all TGF-β treated cells did revert their polarity (Figure 2D, E) to compare the scattering of TGF-β treated cells depending on their pre-established polarity. For this, we used the larger Golgi apparatus rather than small centrosome markers to facilitate their detection by live cell microscopy. We saw a clear difference in scattering behavior of TGF-β treated depending upon the initial orientation of their polarity axis: cells with the polarity axis pointing toward inter-cellular junctions (similar to non-treated epithelial cells) had less propensity (24%, n=25) to separate from each other compared to cells with a polarity axis pointing toward Cell-matrix adhesion (69%, n=43) (Figure 7C and movie S4).

We further attempted to specifically interfere with centrosome repositioning in TGF-b treated cells by reducing microtubule disassembly prior to cell release. Strikingly, cell scattering was reduced by 66% (n=131) in stathmin knock-down cells and by 85% (n=78) in taxol-treated cells compared to the control cells (n=77) (Figure 7D and Movie S5). Noteworthy all cells (Control siRNA, stathmin siRNA and Taxol treatment) formed an intercellular junction when confined, but only cells with stabilized microtubules retained it after release from confinement. These experiments conclusively proved that, upon TGF-β induced EMT, cells that maintained their polarity toward intercellular junction behaved like epithelial cells with less scattering potential while cells with inverted polarity were primed for cell scattering. Hence, we establish that EMT induction involves polarity reversal by centrosome repositioning away from inter-cellular junctions to promote cell separation.

## Discussion

These results have revealed the existence of a global intra-cellular rearrangement occurring in the few hours following the addition of TGF-β, which therefore appeared as one of the earliest morphological sign of EMT that precedes the loss of inter-cellular connections. Microtubule network geometry and centrosome position rapidly adapt to early modifications of inter-cellular junction composition and notably to the reduction of Par3 concentration. Decrease in microtubule nucleation and polymerization in addition to the decrease of selective microtubule stabilization along the junction lead to centrosome displacement from the junction to the cell center (Figure 7E). Thereby the centrosome relocates on the opposite side of the nucleus. These intra-cellular rearrangements result into an effective reversal of internal polarity axis and are coordinated with inversion of cortical polarity component localization such as Par3 and Podocalyxin (Figure 5C, Figure S2G). Centrosome repositioning further promotes cell scattering (Figure 7E). As such, the centrosome-microtubule network appears to act as an extensive and sensitive spatial integrator of cell adhesion cues allowing the orientation of cell internal polarity to adapt to changes in cell's microenvironment.

How the centrosome adopts an off-center position toward inter-cellular junctions in epithelial cells is not well understood. Centrosome decentering is generally considered to rely on the production of pulling forces from a defined part of cell periphery as it has been described during immune synapse formation (Yi et al., 2013) and spindle orientation (Théry et al., 2007). Par3 is present along epithelial cells junctions. It is capable to recruit dynein that pulls on microtubules (Ligon et al., 2001; Schmoranzer et al., 2009) and thereby can direct centrosome position like during planar cell polarity establishment (Jiang et al., 2015; Sipe et al., 2013), intestinal cell polarization (Feldman and Priess, 2012) and neurulation (Buckley et al., 2012; Hong et al., 2010). The correlation we observed between Par3 levels and centrosome position in our conditions (Figure 5C-F) are consistent with this off-centering mechanism.

However, a mechanism based on local pulling only would not be sensitive and efficient as it would have to overcome the centering forces applied on all the other microtubules (Letort et al., 2016). Numerical simulations suggested that some specific reorganizations of microtubule network, including the elongation and increased number of microtubules, could circumvent this limitation by developing decentering pushing forces in the entire network (Letort et al., 2016). Our experimental and numerical experiments are consistent with this view. In epithelial cells, microtubules were long and numerous and the centrosome was off-centered. Whereas in mesenchymal cells microtubules were shorter and less numerous and the centrosome localized at the cell center. Microtubule length increase in mesenchymal cells by down-regulation of stathmin expression level restored centrosome position to an off-centered, epithelial-like, conformation. These observations were also consistent with the previous descriptions of decentered centrosomes in lipid vesicles (Pinot et al., 2009) or microfabricated chambers (Faivre-Moskalenko and Dogterom, 2002) when microtubules were longer than the diameter of the space they were confined in.

The mechanism by which knock down of stathmin prevented microtubule disassembly, centrosome repositioning to the cell center and cell scattering in response to TGF-β is unclear. Stathmin modulates microtubule dynamics via its interaction with tubulin dimers (Belmont and Mitchison, 1996) but, interestingly, also affects microtubule nucleation at the centrosome (Ringhoff and Cassimeris, 2009), which is consistent with our observation of reduced level of γ-tubulin and EB1 at the centrosome upon addition of TGF-β. In parallel, stathmin (also named oncoprotein 18) is known to be overexpressed in several form of human malignancies and has already been suggested to contribute to oncogenic EMT (Li et al., 2011; Lu et al., 2014; Melhems et al., 1991), in which polarity reversal would be worth being investigated.

Importantly, our results show that centrosome-microtubule network geometry adapts to but also actively feedbacks to the adhesion-actin network configuration. TGF-β treated cells that did not undergo polarity reversal could not separate upon the release of spatial constraint suggesting that the centrosome stabilizes the inter-cellular junction as long as it stays close to it and promotes the migration machinery as it comes closer to cell-matrix adhesions at the cell front. Indeed microtubules interact and feedback with both types of adhesions (Akhmanova et al., 2009). The centrosome and the junction exchange materials: some centrosomal proteins transit from centrosome to the junction, allowing local microtubule anchoring and stabilization (Gavilan et al., 2015; Lechler and Fuchs, 2007; Moss et al., 2007). In return, microtubules stabilize the junction (Meng et al., 2008), notably by the dynein-dependent recruitment of intercellular junction components like occludin (Glotfelty et al., 2014). Some translocated centrosomal proteins even promote junction reinforcement and epithelial cell acquisition of a columnar shape (Gavilan et al., 2015). Similarly, when internal polarity axis is directed toward cell adhesion to ECM, microtubule density increases can promote actin polymerization and adhesion turnover and thereby foster cell migration (Etienne-Manneville, 2013). Interestingly, during epithelial scattering occludin and Par3 have been shown to relocalize from inter-cellular junction to the cell front where they promote leading edge protrusion and cell migration (Du et al., 2010). Par3 relocalization was also observed in our working conditions on micropatterns. These considerations account for the capacity of centrosome relocalization from intercellular junction toward ECM adhesions to actively weaken inter-cellular interaction and promote the cell migration machinery even before effective cell displacement and thereby primes cell scattering.

Thus our results provide new evidences for the key role of the centrosome-microtubule network interplay with the adhesion-actin system in the regulation of complex tissue remodeling.

## Experimental Procedures

The description of the details of mouse embryo and mammary gland manipulation, 3D acini formation, cell culture and transfection, DNA constructs, drug treatments, antibodies, micropatterning, microscopy can be found in Supplemental Experimental Procedures.

### Cell culture and EMT induction

MCF10A cells were cultured in Lonza MEGM medium (Lonza #CC3150) as described by ATCC protocol. MDCK, NMuMG and EpH4 cells were cultured as described in Supplemental experimental procedures. EMT was induced by addition of 5 ng/ml TGF-β1 to MCF10A for 5 days, 2 ng/ml to NMuMG & EpH4 for 3 days and 10 ng/ml of HGF for MDCK for 3 days. MCF10A 3D cultures were prepared by cultivating cells in Matrigel as described previously (Debnath et al., 2003).

### Cell micropatterning

Micropatterns were fabricated by coating poly-ethylene-glycol on glass and exposing this coating to deep UV light through a chromium photomask (Azioune et al., 2010). Soft substrates micropatterning was achieved by polymerizing a mix of acrylamide and bis-acrylamide onto a micropatterned glass slide to transfer proteins from the glass onto the hydrogel (Vignaud et al., 2014). Traction forces were calculated with an Image J plugin to measure gel relaxation field after cell detachment (Martiel et al., 2015). Dynamic micropatterning was performed using click chemistry to bind BCN-RGD onto azide groups grafted on PLL-PEG (van Dongen et al., 2013).

### Cell Scattering on line micropatterns and video-microscopy

150,000 cells per were plated onto micropatterned lines on a 20x20 mm glass coverslip. Non attached cells were rinsed away by medium exchange once few cells were attached to the micropattern to avoid obtaining several cells per line. Coverslips were then mounted on video chambers (Chamlide, CM-S20-1). Cells motion was then video-recorded in transmitted light with a Nikon Eclipse Ti-E with 10x phase contrast objective. Time interval was set to 15 min. Cell separation after division was then counted by visual inspection.

### Quantification of centrosome position

Image analysis for centrosome positioning was performed using a series of Macros in Image J. Briefly; z-projection of each color channel was obtained using 'maximum z-projection' plugin followed by merging the 4 channels to obtain a composite image. Using Pattern Alignment plugin (https://sites.google.com/site/qingzongtseng/template-matching-ij-plugin) images were aligned with the reference micropattern image. Nuclei in DAPI channel were detected using image thresh-holding and object size criteria. Centrosomes were detected with similar thresh-holding and by using nuclei Region Of Interest (ROI) as spatial reference. Finally nucleus-centrosome vector was computed by subtracting co-ordinates of centrosome from nucleus co-ordinates and was normalized by the nucleus radius as indicated in Figure 2.

### Quantification of EB1 comets

Z-projected images of EB1 comets were obtained as described above. Background subtraction was

performed using a rolling ball radius of 50. For analyzing nucleation capacity of the centrosome, ROI of 1.5µm radius was drawn around the centrosome labeled by Ninein. EB1 comets were detected in the selected ROI by 'Find Maxima' Process.

**Quantification of microtubule intensity**

Images of microtubules were acquired using CSUX1-A1N Nikon Spinning Disk microscope (Yokogawa) with 100X, 1.3 NA objective and Evolve 512 EMCCD camera (Photometrics). Z-projected images 'Maximum z intensity' of alpha-tubulin staining were obtained as described above. A ROI 46x46 µm was selected containing the cell pair on <H> micropatterns. Total intensity of the image was measured in Image J for each image to quantify total microtubule density in each cell-pair. To quantify microtubule density at the cell-cell junction, a ROI of 3.2 µm thickness was drawn along the cell-cell junction and intensity of alpha-tubulin staining was measured.

**Quantification of acini polarization**

Images of acini were acquired on a Nikon Spinning Disk microscope at 60x oil objective with a z-step of 500 nm. To determine angle alpha formed between normal to cell periphery and the nucleus-centrosome vector (Figure 1), 4-5 central planes of acini images were selected to obtain single layers of cells at the center of the acini. A spatial reference line was drawn along the basal surface of cells, which was marked by phalloidin staining. Using the 'angle' measurement in Image J, the value of alpha (0-180°) was determined providing the angle formed by vectors in the same plane. Only the plane in the middle of acini was considered for these measurements.

**Numerical Simulations using Cytosim Software**

Simulations were performed using the Cytosim software (www.cytosim.org). Microtubules are considered as elastic fibers surrounded by a viscous fluid following Langevin dynamics (Nedelec and Foethke, 2007). We simulated only microtubules nucleated from and anchored to a centrosomal complex. New nucleation of microtubules, microtubules unbinding from centrosome or steric interactions between microtubules are not taken into account. Microtubules can grow at a force-dependent speed, can undergo catastrophe events and shrink, and can undergo rescue events. Their bending elasticity is modelled following Euler's buckling description. Microtubules are initially uniformly distributed around the centrosome and can freely rotate around it. They are constrained into a rectangular space with an Hookean rappel force and will push against this border but can glide freely along it. Cytoplasmic dyneins are modeled as immobile objects spread into the cellular space that can bind/unbind microtubules and move toward the microtubule minus end when bound, thus generating a pulling force on the centrosome.

**Statistical Analysis**

Mann-Whitney non-parametric test was used to compare differences between the samples. Error bars indicate standard error mean (SEM). N indicates numbers of experiments while n indicates sample size.

**Supplemental Information**

Supplemental Information includes Supplemental Experimental Procedures, three figures, and five movies.

**Authors contribution**

M.B. performed most experimental work and data analyses. M.P. performed most experiments with MDCK. S.T. performed experiments on mouse mammary glands. G.B. performed experiments on mouse embryos. Q.T. performed preliminary experiments and contributed to software developments for image analysis. G.L performed numerical simulations. G.B. and S.L. developed image analysis tools. O.F.C. designed experiments on 3D cell culture and provided key information about EMT to the consortium. J.Y. provided critical comments about the work and edited the manuscript. M.T. directed the project, analyzed the data and wrote the manuscript.

**Acknowledgments**

We thank Priscilla Soulie for providing EpH4 cells, James Sillibourne for providing human-Ninein antibody, Benoit Ladoux for providing anti-GM135 antibody, Matthieu Piel and his team for providing APP & BCN-RGD compounds and advices for dynamic patterning and Benoit Vianay for his help with microscopy. We are grateful to Jean-Paul Thierry for interesting discussions, Laurent Blanchoin for his useful comments throughout the project and Maxence Nachury for his thoughtful advices about the potential role of stathmin.

## Figure Legends

**Figure 1. Evidence of polarity reversal at various stages of mouse development and within 3D organotypic cell culture**

(A) Scheme representing germ layers of E8 mouse embryo, site of primitive streak formation and deduced nucleus-centrosome orientations from images in inset 1,2. Inset 1: Posterior end of embryo stained for T-Brachyury (white), γ-tubulin (red) and DAPI (blue). Arrows indicate cells expressing T-Brachyury with nucleus-centrosome axis (white arrows) orientated away from amniotic cavity (marked c). Inset2: Anterior end of E8 mouse showing cells without T-Brachyury and nucleus-centrosome axis pointing toward the amniotic cavity. Scale bar represents 20 μm.

(B) 3D analysis of nucleus-centrosome vectors in embryo using 3D image analysis software.

(C) Quantification of angle $\alpha$ contained by normal to cell base and nucleus-centrosome vector in mesoderm (T-brachyury positive) and Epiblast (T-brachyury negative) cells.

(D) Scheme representing nucleus-Golgi apparatus axis of cells in growing terminal end bud of female mouse mammary gland at 6-7 weeks of age. Inset 1: Merged image of terminal end bud stained for Golgi apparatus (green), F-actin (red) and nucleus (blue). Images of separate channels are below. Scale bar represents 50 μm.

(E) Examples of control and TGF-β treated MCF10A 3D cultures (Day7) labeled for Golgi apparatus (green), centrosome (white), F-actin (green) with zoomed and cropped image showing nucleus-centrosome orientation on the right. Scale bar represents 20 μm.

(F). Scatter plots show quantification of angle $\alpha$ for control and TGF-β treated MCF10A cells. n represents total number of cells quantified from Control (N=23) and TGF-β (N=25) acini. Two tailed-non-parametric Mann-Whitney test was used, ****: p<0.0001.

**Figure 2. Polarity reversal is an early feature of EMT**

(A) Images of nuclei (blue) of MCF10A cell doublets on square (i), bowtie (ii) and H-shaped (iii) microcropatterns (grey). Graphs represent angular distribution of nucleus-nucleus axis (NN axis) orientation of cell doublets. n indicates number of cells.

(B) MCF10A and MDCK cell doublets on H-shaped micropattern were stained for F-actin (green) (top) or centrosome (red) and DNA (blue) (bottom).

(C) Axes system defined by NN axis (X axis) passing through center of nuclei of cell doublets and an axis perpendicular to NN axis (Y axis). Normalized nucleus-centrosome vector coordinates (NCx, NCy) were calculated by subtracting coordinates of centrosome (Cx, Cy) from Nucleus (Nx, Ny) and normalized by the nucleus distance (NR).

(D) Scatter plot of normalized NC vector. The total number of cells and the respective proportions (%) on positive and negative x-axis are indicated.

(E) Horizontal histograms show the quantification of polarity index, i.e normalized X coordinate of NC vector. N indicates the number of independent experiments, whereas n indicates the total number of single cells. Vertical box plots show the quantification of inter-nuclear and inter-centrosome distance.

(F) Polarity index toward cell-cell junction in control (blue) after varying the duration of TGF-β treatment and HGF treatment to MCF10A and MDCK cells.

Two tailed-non-parametric Mann-Whitney tests were used. ****: p<0.0001. Error bars

indicate SEM. See also Figure S2 and S3.

**Figure 3. Matrix stiffness promotes polarity reversal**

(A) Images of control and TGF-β treated EpH4 cell doublets on H-shaped glass micropattern stained for E-cadherin (green), centrosome (red and white arrows) and DNA (blue). Cell doublets on Polyacrylamide gel were labeled for F-actin (green).

(B) Control NMuMG cells on glass and polyacrylamide gels are stained for Giantin (Golgi apparatus marker) (red), F-actin(green) and DNA (blue). Horizontal histograms show quantification of polarity index toward cell-cell junction. Scale bars represent 5 μm. Errors bar indicate SEM. Two tailed-non-parametric Mann-Whitney tests were used. ****: p<0.0001. Error bars indicate SEM.

**Figure 4. Microtubule network remodeling accompanies centrosome re-centering during EMT**

(A) Images of control and TGF-β treated MCF10A cell-doublets on H-shaped micropattern stained for -tubulin. Box plot shows quantification of total microtubule density on left. Microtubule density in two populations TGF-β treated cells with different nucleus-centrosome axis polarity on right. (AU is arbitrary fluorescence units).

(B) Images of MCF10A cell-doublets stained for EB1. Scatter plots show quantification of total EB1 comets, EB1 comets at the centrosome and γ-tubulin at the centrosome. A circular region of interest of 1.5 μm radius (red dotted circle) was used to count EB1 comets and γ-tubulin intensity at the centrosome.

(C) Numerical simulation showing microtubules (white) and centrosome (yellow) motion in response to varying microtubules number in a rectangular cell. Green dots correspond to cytoplasmic dynein (green).

(D) Effect of varying microtubule number on centrosome trajectory to final position. Different colors represent different microtubule number. Graph represents relationship between number of microtubules and the final position of the centrosome relative to cell center.

(E) Centrosome trajectories when starting from various initial positions (marked by cross) for either 100 (top) or 250 (bottom) microtubules.

(F) Images of TGF-β treated and stathmin knocked down cells with microtubules (white), nuclei (blue). Total Microtubule density (Arbitrary units) of stathmin knocked down cells. Scale bar (A-F) is 10 μm

(G) Images of TGF-β treated acini transfected with siRNA. Nucleus-golgi axis orientation (α) with respect to normal to the base of acini is quantified.

(H) Images of TGF-β treated cells with 5 hours of Taxol treatment. Polarity index is quantified on right. Scale bar is 10 μm.

Two tailed-non-parametric Mann-Whitney tests were used. ***: p<0.001, ****: p<0.0001.

**Figure 5. Par3 regulates centrosome position during EMT**

(A) Microtubule density and EB1 comets at the cell-cell junction are measured within the area indicated by red dotted lines of MCF10A cells on H-micropattern. AU is arbitrary units.

(B) Density of acetylated microtubules was measured at the cell-cell junction in the area marked by red dotted lines in panel (A).
(C) Par3 (green), γ-tubulin (red) and DNA (blue) staining of MCF10A cells. Central graph shows the relationship between Par3 enrichment at cell-cell junction and inter-centrosome distance. Pearson's correlation test r, ****: p<0.001, *: p<0.1, ns>0.1.
(D) Vertical histograms show measurement of polarity index toward cell-cell junction.
(E) Image of Par3 siRNA treated control cells and TGF-β treated cells with Par3 overexpression, labeled for Par3 (green), centrosome (red) and DNA (blue). Box plots show quantification of inter-centrosome distance.
(F) Horizontal histogram shows quantification of cell polarity index toward cell-cell junction. Arrows point at centrosomes. Scale bars represent 10 μm. Errors bar indicate SEM. Two tailed-non-parametric Mann-Whitney test were used ***:p<0.001, ****:p<0.0001.

**Figure 6. Centrosome repositioning promotes cells scattering during EMT**
(A) Time-lapse sequence NMuMG cells (red arrows) on micro-patterned lines. Quantification of the proportion of cell separation in control and TGF-β treated cells for various cell types. n indicates number events measured for cell separation.
(B) Images of fixed NMuMG cells labeled for F-actin (green) and nucleus (blue) on micropatterned tracks of 300 μm. Histograms show the quantification of inter-nuclear distance between cell pairs of different cell lines.
(C) Images of TGF-β treated MCF10A cell-pairs on micropatterned tracks in different configurations of nucleus-centrosome axis orientation. Arrows indicate centrosomes. The proportion of each configuration is quantified on right.
(D) Images of TGF-β treated MCF10A cell-pairs in the presence of DMSO or Taxol (5 hours of treatment) and cells transfected with control or stathmin siRNA. On the right inter-nuclear distances between the cell-pairs are quantified.

**Figure 7. Polarity reversal is necessary for cell scattering**
(A) Schematic depicting principle of dynamic micropatterning with azide-PLL-PEG (orange) and cell motion on BCN-RGD modified substrate (red).
(B) Images of cells on H-shaped micropattern before and after modification of BCN-RGD modified substrate. Histograms show measurement of the proportion of cell separation and maximum inter-nuclear distance between the MCF10A cells two hours after addition of BCN-RGD.
(C) Time-lapse sequence images of TGF-β treated MCF10A cells expressing Golgi apparatus markers (visualized in green at t=0) in response to the addition of BCN-RGD. Histogram shows measurement of the proportion of cell separation depending on their initial polarity orientation. Scale bar is 10 μm.
(D) Time-lapse image sequence of TGF-β treated MCF10A cells with stathmin knockdown or Taxol treatment. Their cell separation post 20 hours of BCN-RGD addition was quantified on right. Scale bar is 10 μm.
(E) Schematic description of microtubule reorganization and centrosome repositioning that causes polarity reversal and finally cell separation during the course of EMT.

# References


Acloque, H., Adams, M.S., Fishwick, K., Bronner-Fraser, M., and Nieto, M.A. (2009). Epithelial-mesenchymal transitions: the importance of changing cell state in development and disease. J. Clin. Invest. *119*, 1438–1449.

Akhmanova, A., Stehbens, S.J., and Yap, A.S. (2009). Touch, grasp, deliver and control: functional cross-talk between microtubules and cell adhesions. Traffic *10*, 268–274.

Akhtar, N., and Streuli, C.H. (2013). An integrin-ILK-microtubule network orients cell polarity and lumen formation in glandular epithelium. Nat. Cell Biol. *15*, 17–27.

Anstrom, J.A., and Raff, R.A. (1988). Sea urchin primary mesenchyme cells: Relation of cell polarity to the epithelial-mesenchymal transformation. Dev. Biol. *130*, 57–66.

Azioune, A., Carpi, N., Tseng, Q., Théry, M., and Piel, M. (2010). Protein micropatterns: A direct printing protocol using deep UVs. Methods Cell Biol. *97*, 133–146.

Belmont, L.D., and Mitchison, T.J. (1996). Identification of a protein that interacts with tubulin dimers and increases the catastrophe rate of microtubules. Cell *84*, 623–631.

Bornens, M. (2008). Organelle positioning and cell polarity. Nat. Rev. Mol. Cell Biol. *9*, 874–886.

Bryant, D.M., Roignot, J., Datta, A., Overeem, A.W., Kim, M., Yu, W., Peng, X., Eastburn, D.J., Ewald, A.J., Werb, Z., et al. (2014). A Molecular Switch for the Orientation of Epithelial Cell Polarization. Dev. Cell *31*, 171–187.

Buckley, C.E., Ren, X., Ward, L.C., Girdler, G.C., Araya, C., Green, M.J., Clark, B.S., Link, B. a, and Clarke, J.D.W. (2012). Mirror-symmetric microtubule assembly and cell interactions drive lumen formation in the zebrafish neural rod. EMBO J. *32*, 30–44.

Burute, M., and Thery, M. (2012). Spatial segregation between cell-cell and cell-matrix adhesions. Curr. Opin. Cell Biol. *24*, 628–636.

Carney, P.R., and Couve, E. (1989). Cell polarity changes and migration during early development of the avian peripheral auditory system. Anat. Rec. *225*, 156–164.

D'Souza, R., Knittle, a. M., Nagaraj, N., van Dinther, M., Choudhary, C., ten Dijke, P., Mann, M., and Sharma, K. (2014). Time-resolved dissection of early phosphoproteome and ensuing proteome changes in response to TGF-. Sci. Signal. *7*, rs5-rs5.

Das, R.M., and Storey, K.G. (2014). Apical abscission alters cell polarity and dismantles the primary cilium during neurogenesis. Science (80-. ). *343*, 200–204.

Debnath, J., Muthuswamy, S.K., and Brugge, J.S. (2003). Morphogenesis and oncogenesis of MCF-10A mammary epithelial acini grown in three-dimensional basement membrane cultures. Methods *30*, 256–268.

Desai, R.A., Gao, L., Raghavan, S., Liu, W.F., and Chen, C.S. (2009). Cell polarity triggered by cell-cell adhesion via E-cadherin. J. Cell Sci.

van Dongen, S.F.M., Maiuri, P., Marie, E., Tribet, C., and Piel, M. (2013). Triggering cell adhesion, migration or shape change with a dynamic surface coating. Adv. Mater. *25*, 1687–1691.

Du, D., Xu, F., Yu, L., Zhang, C., Lu, X., Yuan, H., Huang, Q., Zhang, F., Bao, H., Jia, L., et al. (2010). The tight junction protein, occludin, regulates the directional migration of epithelial cells. Dev. Cell *18*, 52–63.

Etienne-Manneville, S. (2013). Microtubules in cell migration. Annu. Rev. Cell Dev. Biol. *29*, 471–499.

Ewald, A.J., Brenot, A., Duong, M., Chan, B.S., and Werb, Z. (2008). Collective Epithelial Migration and Cell Rearrangements Drive Mammary Branching Morphogenesis. Dev. Cell *14*, 570–581.

Faivre-Moskalenko, C., and Dogterom, M. (2002). Dynamics of microtubule asters in microfabricated chambers: the role of catastrophes. Proc. Natl. Acad. Sci. U. S. A. *99*, 16788–16793.

Feldman, J.L., and Priess, J.R. (2012). A role for the centrosome and PAR-3 in the hand-off of MTOC function during epithelial polarization. Curr. Biol. *22*, 575–582.

Filbert, E.L., Le Borgne, M., Lin, J., Heuser, J.E., and Shaw, A.S. (2012). Stathmin regulates microtubule dynamics and microtubule organizing center polarization in activated T cells. J. Immunol. *188*, 5421–5427.

Gavilan, M.P., Arjona, M., Zurbano, A., Formstecher, E., Martinez-Morales, J.R., Bornens, M., and Rios, R.M. (2015). Alpha-catenin-Dependent Recruitment of the Centrosomal Protein CAP350 to Adherens Junctions Allows Epithelial Cells to Acquire a Columnar Shape. PLOS Biol. *13*, e1002087.

Glotfelty, L. a, Zahs, A., Iancu, C., Shen, L., and Hecht, G. a (2014). Microtubules Are Required for Efficient Epithelial Tight Junction Homeostasis and Restoration. Am. J. Physiol. Cell Physiol. *307*, 245–254.

Godde, N.J., Galea, R.C., Elsum, I. a, and Humbert, P.O. (2010). Cell polarity in motion: redefining mammary tissue organization through EMT and cell polarity transitions. J. Mammary Gland Biol. Neoplasia *15*, 149–168.

Harris, T.J.C., and Peifer, M. (2007). aPKC controls microtubule organization to balance adherens junction symmetry and planar polarity during development. Dev. Cell *12*, 727–738.

Hebert, A.M., Duboff, B., Casaletto, J.B., Gladden, A.B., and McClatchey, A.I. (2012). Merlin/ERM proteins establish cortical asymmetry and centrosome position. Genes Dev. *26*, 2709–2723.

Higginbotham, H.R., and Gleeson, J.G. (2007). The centrosome in neuronal development. Trends Neurosci. *30*, 276–283.

Hinck, L., and Silberstein, G.B. (2005). Key stages in mammary gland development: the mammary end bud as a motile organ. Breast Cancer Res. *7*, 245–251.

Hong, E., Jayachandran, P., and Brewster, R. (2010). The polarity protein Pard3 is required for centrosome positioning during neurulation. Dev. Biol. *341*, 335–345.

Huang, R.Y.-J., Guilford, P., and Thiery, J.P. (2012). Early events in cell adhesion and polarity during epithelial-mesenchymal transition. J. Cell Sci. 4417–4422.

Inman, G.J., Nicolás, F.J., Callahan, J.F., Harling, J.D., Gaster, L.M., Reith, A.D., Laping, N.J., and Hill, C.S. (2002). SB-431542 is a potent and specific inhibitor of transforming growth factor-beta superfamily type I activin receptor-like kinase (ALK) receptors ALK4, ALK5, and ALK7. Mol. Pharmacol. *62*, 65–74.

Jiang, T., McKinley, R.F.A., McGill, M.A., Angers, S., and Harris, T.J.C. (2015). A Par-1-Par-3-Centrosome Cell Polarity Pathway and Its Tuning for Isotropic Cell Adhesion. Curr. Biol. *25*, 2701–2708.

Lamouille, S., and Derynck, R. (2007). Cell size and invasion in TGF-beta-induced epithelial to mesenchymal transition is regulated by activation of the mTOR pathway. J. Cell Biol. *178*, 437–451.

Lamouille, S., Xu, J., and Derynck, R. (2014). Molecular mechanisms of epithelial-mesenchymal transition. Nat. Rev. Mol. Cell Biol. *15*, 178–196.

Lechler, T., and Fuchs, E. (2007). Desmoplakin: an unexpected regulator of microtubule organization in the epidermis. J. Cell Biol. *176*, 147–154.

Letort, G., Nedelec, F., Blanchoin, L., and Théry, M. (2016). Centrosome centering and decentering by microtubule network rearrangement. Mol. Biol. Cell *27*, 2833–2843.

Li, N., Jiang, P., Du, W., Wu, Z., Li, C., Qiao, M., Yang, X., and Wu, M. (2011). Siva1 suppresses epithelial-mesenchymal transition and metastasis of tumor cells by inhibiting stathmin and stabilizing microtubules. Proc. Natl. Acad. Sci. U. S. A. *108*, 12851–12856.

Ligon, L.A., Karki, S., Tokito, M., and Holzbaur, E.L.F. (2001). Dynein binds to β -catenin and may tether microtubules at adherens junctions. Nat. Cell Biol. *3*, 913–917.

Lu, Y., Liu, C., Xu, Y.F., Cheng, H., Shi, S., Wu, C.T., and Yu, X.J. (2014). Stathmin destabilizing microtubule dynamics promotes malignant potential in cancer cells by epithelial-mesenchymal transition. Hepatobiliary Pancreat. Dis. Int. *13*, 386–394.

Luxton, G.W.G., and Gundersen, G.G. (2011). Orientation and function of the nuclear-centrosomal axis during cell migration. Curr. Opin. Cell Biol. *23*, 579–588.

Markowski, M.C., Brown, A.C., and Barker, T.H. (2012). Directing epithelial to mesenchymal transition through engineered microenvironments displaying orthogonal adhesive and mechanical cues. J. Biomed. Mater. Res. - Part A *100 A*, 2119–2127.

Martiel, J.-L., Leal, A., Kurzawa, L., Balland, M., Wang, I., Vignaud, T., Tseng, Q., and Théry, M. (2015). Measurement of cell traction forces with ImageJ. Methods Cell Biol. *125*, 269–287.

Melhems, R.F., Zhu, X., Hailat, N., Strahler, J.R., and Hanash, S.M. (1991). Characterization of the Gene for a Proliferation-related. *266*, 17747–17753.

Meng, W., Mushika, Y., Ichii, T., and Takeichi, M. (2008). Anchorage of microtubule minus ends to adherens junctions regulates epithelial cell-cell contacts. Cell *135*, 948–959.

Mimori-Kiyosue, Y. (2011). Shaping microtubules into diverse patterns: Molecular connections for setting up both ends. Cytoskeleton *68*, 603–618.

Montesano, R., Carrozzino, F., and Soulié, P. (2007). Low concentrations of transforming growth factor-beta-1 induce tubulogenesis in cultured mammary epithelial cells. BMC Dev. Biol. *7*, 7.

Moss, D.K., Bellett, G., Carter, J.M., Liovic, M., Keynton, J., Prescott, A.R., Lane, E.B., and Mogensen, M.M. (2007). Ninein is released from the centrosome and moves bi-directionally along microtubules. J. Cell Sci. *120*, 3064–3074.

Nedelec, F., and Foethke, D. (2007). Collective Langevin dynamics of flexible cytoskeletal fibers. New J. Phys. *9*, 427–427.

Nelson, W.J. (2009). Remodeling epithelial cell organization: transitions between front-rear and apical-basal polarity. Cold Spring Harb. Perspect. Biol. *1*, a000513.

Nitsch, L., and Wollman, S.H. (1980). Ultrastructure of intermediate stages in polarity reversal of thyroid epithelium in follicles in suspension culture. J.Cell Biol. *86*, 875–880.

Ojakian, K.G., and Schwimmer, R. (1994). Regulation of epithelial cell surface polarity reversal by beta 1 integrins. J. Cell Sci. *107*, 561–576.

Oliaro, J., Van Ham, V., Sacirbegovic, F., Pasam, A., Bomzon, Z., Pham, K., Ludford-Menting, M.J., Waterhouse, N.J., Bots, M., Hawkins, E.D., et al. (2010). Asymmetric Cell Division of T Cells upon Antigen Presentation Uses Multiple Conserved Mechanisms. J. Immunol. *185*, 367–375.

Pinot, M., Chesnel, F., Kubiak, J.Z., Arnal, I., Nedelec, F.J., and Gueroui, Z. (2009). Effects of confinement on the self-organization of microtubules and motors. Curr. Biol. *19*, 954–960.

Pollack, A.L., Runyan, R.B., and Mostov, K.E. (1998). Morphogenetic Mechanisms of Epithelial Tubulogenesis : MDCK Cell Polarity Is Transiently Rearranged without Loss of Cell – Cell Contact during Scatter Factor / Hepatocyte Growth. Dev. Biol. *79*, 64–79.

Pouthas, F., Girard, P., Lecaudey, V., Ly, T.B.N., Gilmour, D., Boulin, C., Pepperkok, R., and Reynaud, E.G. (2008). In migrating cells, the Golgi complex and the position of the centrosome depend on geometrical constraints of the substratum. J. Cell Sci. *121*, 2406–2414.

Revenu, C., Streichan, S., Donà, E., Lecaudey, V., Hufnagel, L., and Gilmour, D. (2014). Quantitative cell polarity imaging defines leader-to-follower transitions during collective migration and the key role of microtubule-dependent adherens junction formation. Development *141*, 1282–1291.

Ringhoff, D.N., and Cassimeris, L. (2009). Abl tyrosine kinase phosphorylates nonmuscle Myosin light chain kinase to regulate endothelial barrier function. Mol. Biol. Cell *20*, 3451–3458.

Rodriguez-Boulan, E., and Macara, I.G. (2014). Organization and execution of the epithelial polarity programme. Nat. Rev. Mol. Cell Biol. *15*, 225–242.

Rodriguez-Fraticelli, A.E., Auzan, M., Alonso, M. a, Bornens, M., and Martin-Belmonte, F. (2012). Cell confinement controls centrosome positioning and lumen initiation during epithelial morphogenesis. J. Cell Biol. *198*, 1011–1023.

Scarpa, E., Szabó, A., Bibonne, A., Theveneau, E., Parsons, M., and Mayor, R. (2015). Cadherin Switch during EMT in Neural Crest Cells Leads to Contact Inhibition of Locomotion via Repolarization of Forces. Dev. Cell *34*, 421–434.

Schmoranzer, J., Fawcett, J.P., Segura, M., Tan, S., Vallee, R.B., Pawson, T., and Gundersen, G.G. (2009). Par3 and dynein associate to regulate local microtubule dynamics and centrosome

orientation during migration. Curr. Biol. *19*, 1065–1074.

Seton-Rogers, S.E., Lu, Y., Hines, L.M., Koundinya, M., LaBaer, J., Muthuswamy, S.K., and Brugge, J.S. (2004). Cooperation of the ErbB2 receptor and transforming growth factor beta in induction of migration and invasion in mammary epithelial cells. Proc. Natl. Acad. Sci. U. S. A. *101*, 1257–1262.

Sipe, C.W., Liu, L., Lee, J., Grimsley-Myers, C., and Lu, X. (2013). Lis1 mediates planar polarity of auditory hair cells through regulation of microtubule organization. Development *140*, 1785–1795.

Solecki, D.J., Trivedi, N., Govek, E.-E., Kerekes, R. a, Gleason, S.S., and Hatten, M.E. (2009). Myosin II motors and F-actin dynamics drive the coordinated movement of the centrosome and soma during CNS glial-guided neuronal migration. Neuron *63*, 63–80.

St Johnston, D., and Sanson, B. (2011). Epithelial polarity and morphogenesis. Curr. Opin. Cell Biol. *23*, 540–546.

Takesono, A., Heasman, S.J., Wojciak-Stothard, B., Garg, R., and Ridley, A.J. (2010). Microtubules regulate migratory polarity through Rho/ ROCK signaling in T cells. PLoS One *5*.

Tam, P.P., and Behringer, R.R. (1997). Mouse gastrulation: the formation of a mammalian body plan. Mech. Dev. *68*, 3–25.

Tang, N., and Marshall, W.F. (2012). Centrosome positioning in vertebrate development. J. Cell Sci. *125*, 4951–4961.

Théry, M. (2010). Micropatterning as a tool to decipher cell morphogenesis and functions. J. Cell Sci. *123*, 4201–4213.

Théry, M., Jiménez-Dalmaroni, A., Racine, V., Bornens, M., and Jülicher, F. (2007). Experimental and theoretical study of mitotic spindle orientation. Nature *447*, 493–496.

Tseng, Q., Duchemin-Pelletier, E., Deshiere, A., Balland, M., Guillou, H., Filhol, O., and Théry, M. (2012). Spatial organization of the extracellular matrix regulates cell-cell junction positioning. Proc. Natl. Acad. Sci. U. S. A. *109*, 1506–1511.

Vignaud, T., Ennomani, H., and Théry, M. (2014). Polyacrylamide hydrogel micropatterning. Methods Cell Biol. *120*, 93–116.

Wang, H., Lacoche, S., Huang, L., Xue, B., and Muthuswamy, S.K. (2013). Rotational motion during three-dimensional morphogenesis of mammary epithelial acini relates to laminin matrix assembly. Proc. Natl. Acad. Sci. *110*, 163–168.

Wang, Z.A., Ojakian, K.G., and Nelson, W.J. (1990). Steps in the morphogenesis of a polarized epithelium II. Disassembly and assembly of plasma membrane domains during reversal of epithelial cell polarity in multicellular epithelial (MDCK) cysts. J. Cell Sci. *95*, 153–165.

Wei, S.C., Fattet, L., Tsai, J.H., Guo, Y., Pai, V.H., Majeski, H.E., Chen, A.C., Sah, R.L., Taylor, S.S., Engler, A.J., et al. (2015). Matrix stiffness drives epithelial–mesenchymal transition and tumour metastasis through a TWIST1–G3BP2 mechanotransduction pathway. Nat. Cell Biol. *17*, 678–688.

Wu, J., Misra, G., Russell, R.J., Ladd, A.J.C., Lele, T.P., and Dickinson, R.B. (2011). Effects of dynein on microtubule mechanics and centrosome positioning. Mol. Biol. Cell *22*, 4834–4841.

Xu, J., Lamouille, S., and Derynck, R. (2009). TGF-beta-induced epithelial to mesenchymal transition. Cell Res. *19*, 156–172.

Yi, J., Wu, X., Chung, A.H., Chen, J.K., Kapoor, T.M., and Hammer, J. a (2013). Centrosome

repositioning in T cells is biphasic and driven by microtubule end-on capture-shrinkage. J. Cell Biol. *202*, 779–792.

Yoo, S.K., Lam, P. -y., Eichelberg, M.R., Zasadil, L., Bement, W.M., and Huttenlocher, A. (2012). The role of microtubules in neutrophil polarity and migration in live zebrafish. J. Cell Sci. *125*, 5702–5710.

Yu, W., O'Brien, L.E., Wang, F., Bourne, H., Mostov, K.E., and Zegers, M.M.P. (2003). Hepatocyte growth factor switches orientation of polarity and mode of movement during morphogenesis of multicellular epithelial structures. Mol. Biol. Cell *14*, 748–763.

Yu, W., Datta, A., Leroy, P., O'Brien, L.E., Mak, G., Jou, T.-S., Matlin, K.S., Mostov, K.E., and Zegers, M.M.P. (2005). Beta1-integrin orients epithelial polarity via Rac1 and laminin. Mol. Biol. Cell *16*, 433–445.

Yvon, A.C., Walker, J.W., Danowski, B., Fagerstrom, C., Khodjakov, A., and Wadsworth, P. (2002). Centrosome Reorientation in Wound-Edge Cells Is Cell Type Specific. Mol. Biol. Cell *13*, 1871–1880.

Zhang, D., Grode, K.D., Stewman, S.F., Diaz-Valencia, J.D., Liebling, E., Rath, U., Riera, T., Currie, J.D., Buster, D.W., Asenjo, A.B., et al. (2011). Drosophila katanin is a microtubule depolymerase that regulates cortical-microtubule plus-end interactions and cell migration. Nat. Cell Biol. *13*, 361–370.

Zhang, J., Tian, X.-J., Zhang, H., Teng, Y., Li, R., Bai, F., Elankumaran, S., and Xing, J. (2014). TGF-β-induced epithelial-to-mesenchymal transition proceeds through stepwise activation of multiple feedback loops. Sci. Signal. *7*, ra91.

# Figure 1

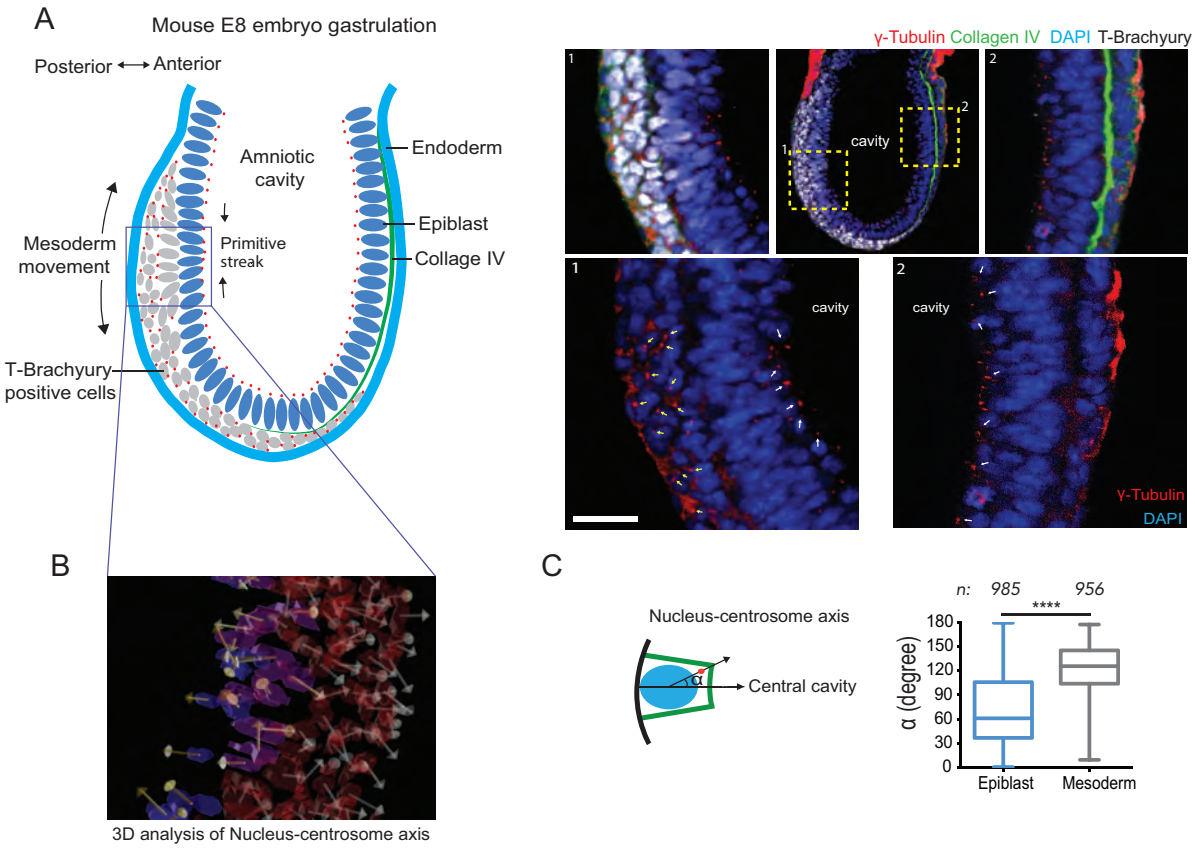
A
Mouse E8 embryo gastrulation
Posterior ⟷ Anterior
Amniotic cavity
Endoderm
Epiblast
Collage IV
Primitive streak
Mesoderm movement
T-Brachyury positive cells
γ-Tubulin Collagen IV DAPI T-Brachyury
cavity
γ-Tubulin
DAPI
B
3D analysis of Nucleus-centrosome axis
C
Nucleus-centrosome axis
Central cavity
α
n: 985 956
****
α (degree)
180
150
120
90
60
30
0
Epiblast
Mesoderm
D
TEB movement
Actin
Lumen
Golgi
Actin Giantin DAPI
Actin
Giantin
DAPI
E
Giantin Actin Ninein DAPI
Zoom in
Control
TGF-β
F
n: 233 200
****
α (degree)
180
150
120
90
60
30
0
Control
TGF-β

# Figure 2

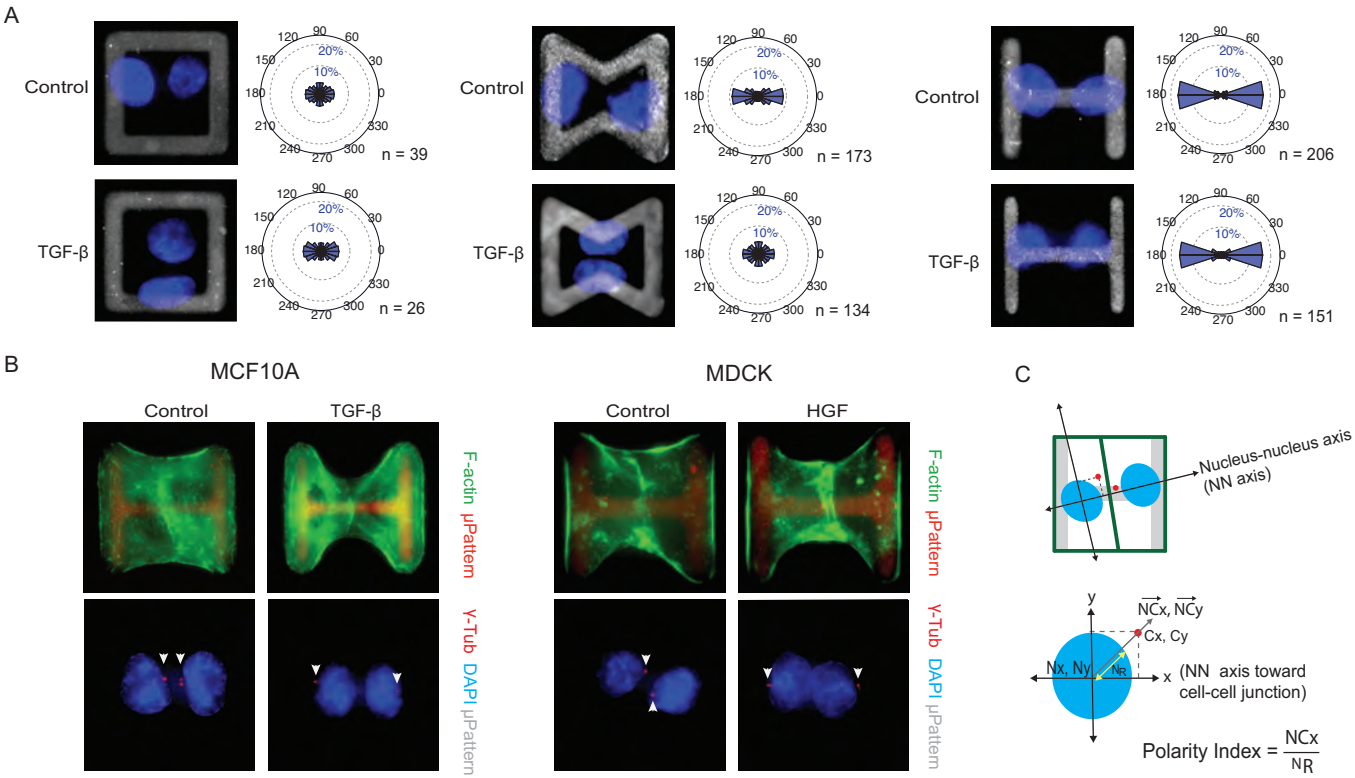
A
Control
TGF-β
n = 39
n = 26
Control
TGF-β
n = 173
n = 134
Control
TGF-β
n = 206
n = 151
B
MCF10A
Control
TGF-β
MDCK
Control
HGF
F-actin μPattern
γ-Tub DAPI μPattern
C
Nucleus-nucleus axis
(NN axis)
(NN axis toward
cell-cell junction)
Polarity Index = NCx / NR
D
MCF10A
MDCK
Control
TGF-β
HGF
28%
72%
68%
32%
43%
57%
57%
43%
n=662
n=700
n=458
n=458
E
MCF10A
MDCK
n: 665, N=8
n: 709 , N=7
n: 458, N=5
n: 494, N=5
TGF-β
HGF
Control
Polarity Index
toward cell-cell junction
Control (n: 625)
TGF-β (n: 285 )
Control (n: 287)
HGF (n: 210)
Distance (μm)
ns
****
internuclear
intercentrosomal
F
MCF10A
MDCK
TGF-β
HGF
5 Day
20 Hour
8 Hour
Control
3 Day
24 Hour
6 Hour
4 Hour
2 Hour
Polarity Index toward cell-cell junction

# Figure 3

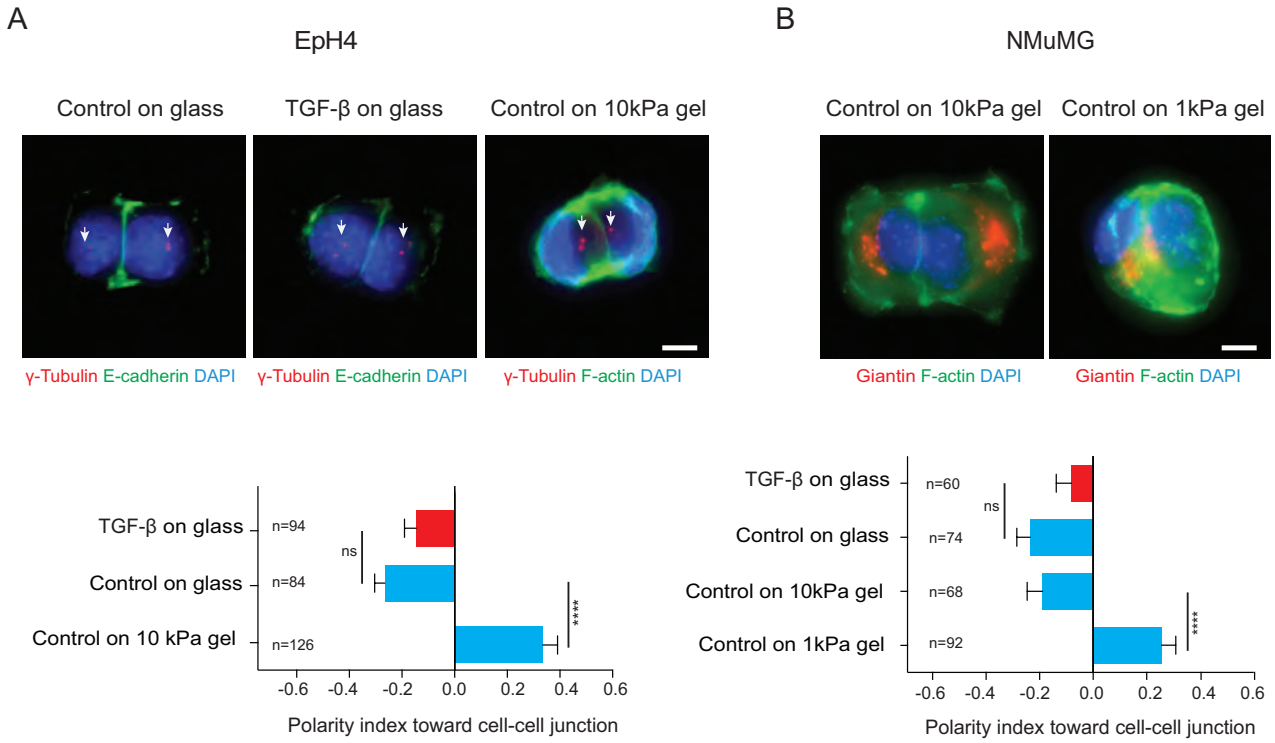
A
EpH4
Control on glass
TGF-β on glass
Control on 10kPa gel
γ-Tubulin E-cadherin DAPI
γ-Tubulin E-cadherin DAPI
γ-Tubulin F-actin DAPI
TGF-β on glass
Control on glass
Control on 10 kPa gel
n=94
n=84
n=126
ns
****
-0.6 -0.4 -0.2 0.0 0.2 0.4 0.6
Polarity index toward cell-cell junction
B
NMuMG
Control on 10kPa gel
Control on 1kPa gel
Giantin F-actin DAPI
Giantin F-actin DAPI
TGF-β on glass
Control on glass
Control on 10kPa gel
Control on 1kPa gel
n=60
n=74
n=68
n=92
ns
****
-0.6 -0.4 -0.2 0.0 0.2 0.4 0.6
Polarity index toward cell-cell junction

# Figure 4

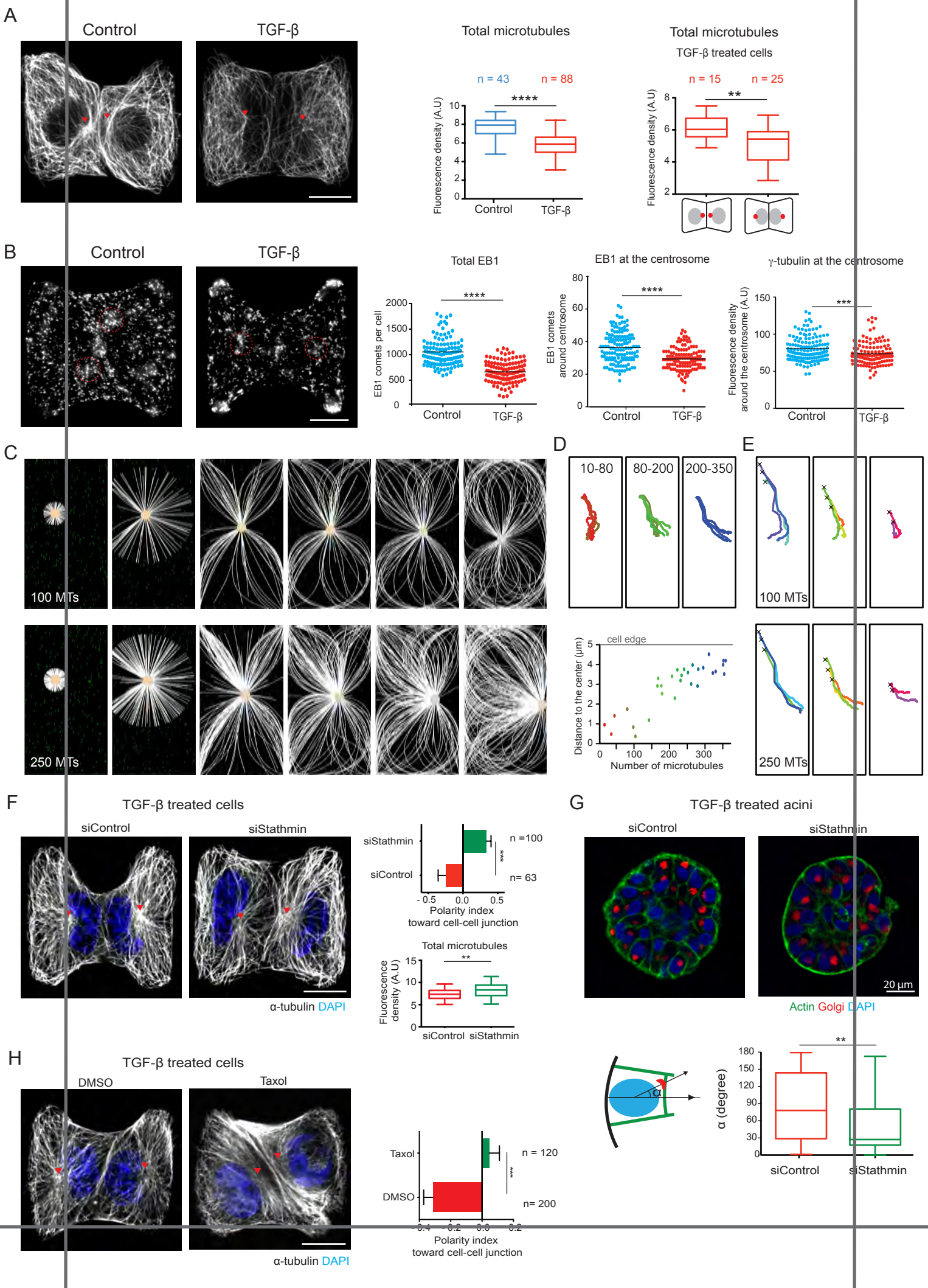
A
Control
TGF-β
Total microtubules
n = 43
n = 88
****
Fluorescence density (A.U)
Control
TGF-β
Total microtubules
TGF-β treated cells
n = 15
n = 25
**
B
Control
TGF-β
Total EB1
EB1 comets per cell
EB1 at the centrosome
EB1 comets around centrosome
γ-tubulin at the centrosome
Fluorescence density around the centrosome (A.U)
***
C
100 MTs
250 MTs
D
10-80
80-200
200-350
cell edge
Distance to the center (μm)
Number of microtubules
E
100 MTs
250 MTs
F
TGF-β treated cells
siControl
siStathmin
n =100
n= 63
Polarity index
toward cell-cell junction
Total microtubules
Fluorescence density (A.U)
α-tubulin DAPI
G
TGF-β treated acini
siControl
siStathmin
20 μm
Actin Golgi DAPI
α
α (degree)
H
TGF-β treated cells
DMSO
Taxol
n = 120
n= 200
Polarity index
toward cell-cell junction
α-tubulin DAPI

# Figure 5

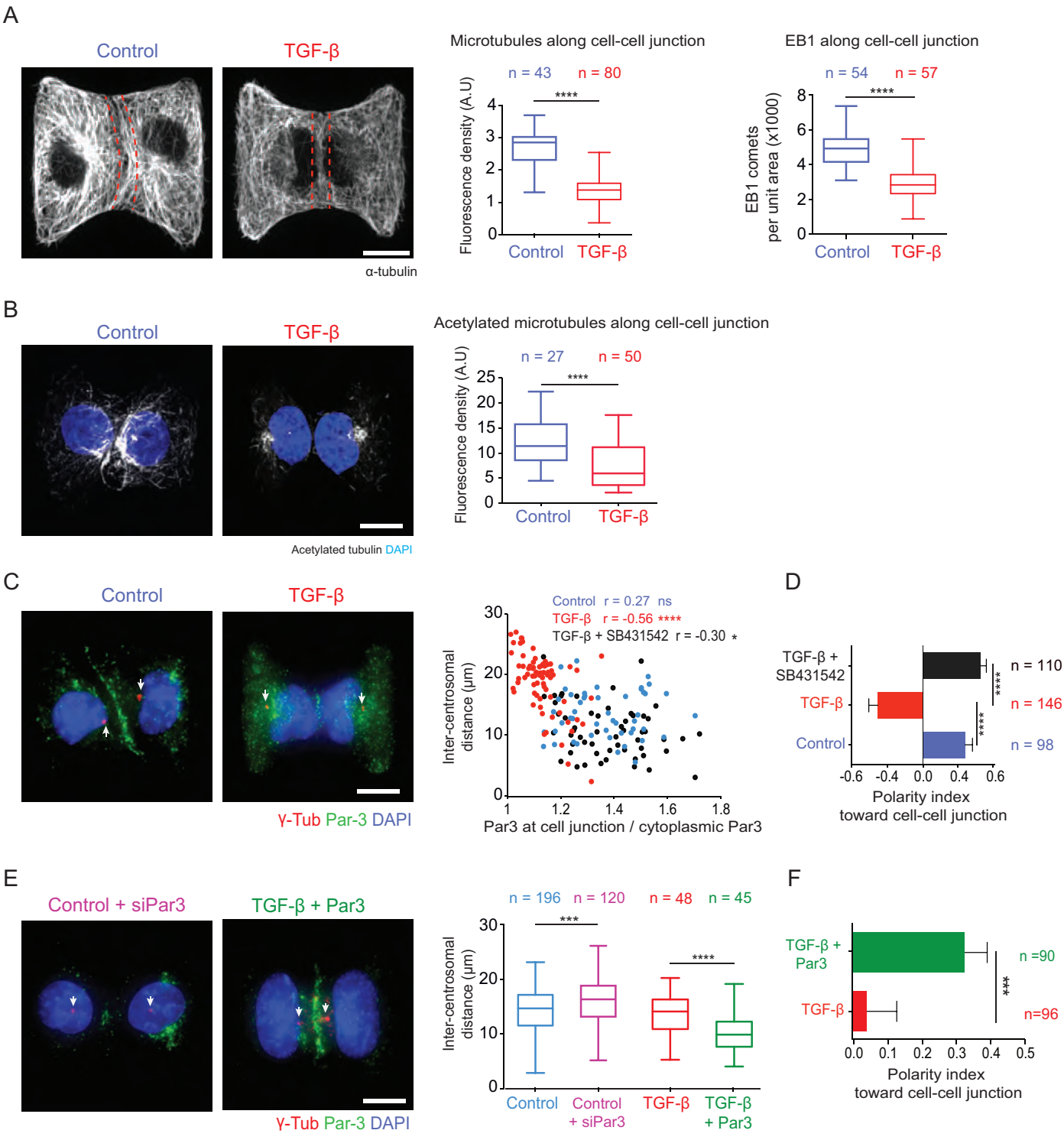
A
Control
TGF-β
α-tubulin
Microtubules along cell-cell junction
n = 43
n = 80
****
Fluorescence density (A.U)
Control
TGF-β
EB1 along cell-cell junction
n = 54
n = 57
****
EB1 comets per unit area (x1000)
B
Control
TGF-β
Acetylated tubulin DAPI
Acetylated microtubules along cell-cell junction
n = 27
n = 50
****
C
Control
TGF-β
γ-Tub Par-3 DAPI
Control r = 0.27 ns
TGF-β r = -0.56 ****
TGF-β + SB431542 r = -0.30 *
Inter-centrosomal distance (µm)
Par3 at cell junction / cytoplasmic Par3
D
TGF-β + SB431542
TGF-β
Control
n = 110
n = 146
n = 98
****
Polarity index toward cell-cell junction
E
Control + siPar3
TGF-β + Par3
γ-Tub Par-3 DAPI
n = 196
n = 120
n = 48
n = 45
***
****
Control
Control + siPar3
TGF-β
TGF-β + Par3
F
TGF-β + Par3
TGF-β
n =90
n=96
***
Polarity index toward cell-cell junction

# Figure 6

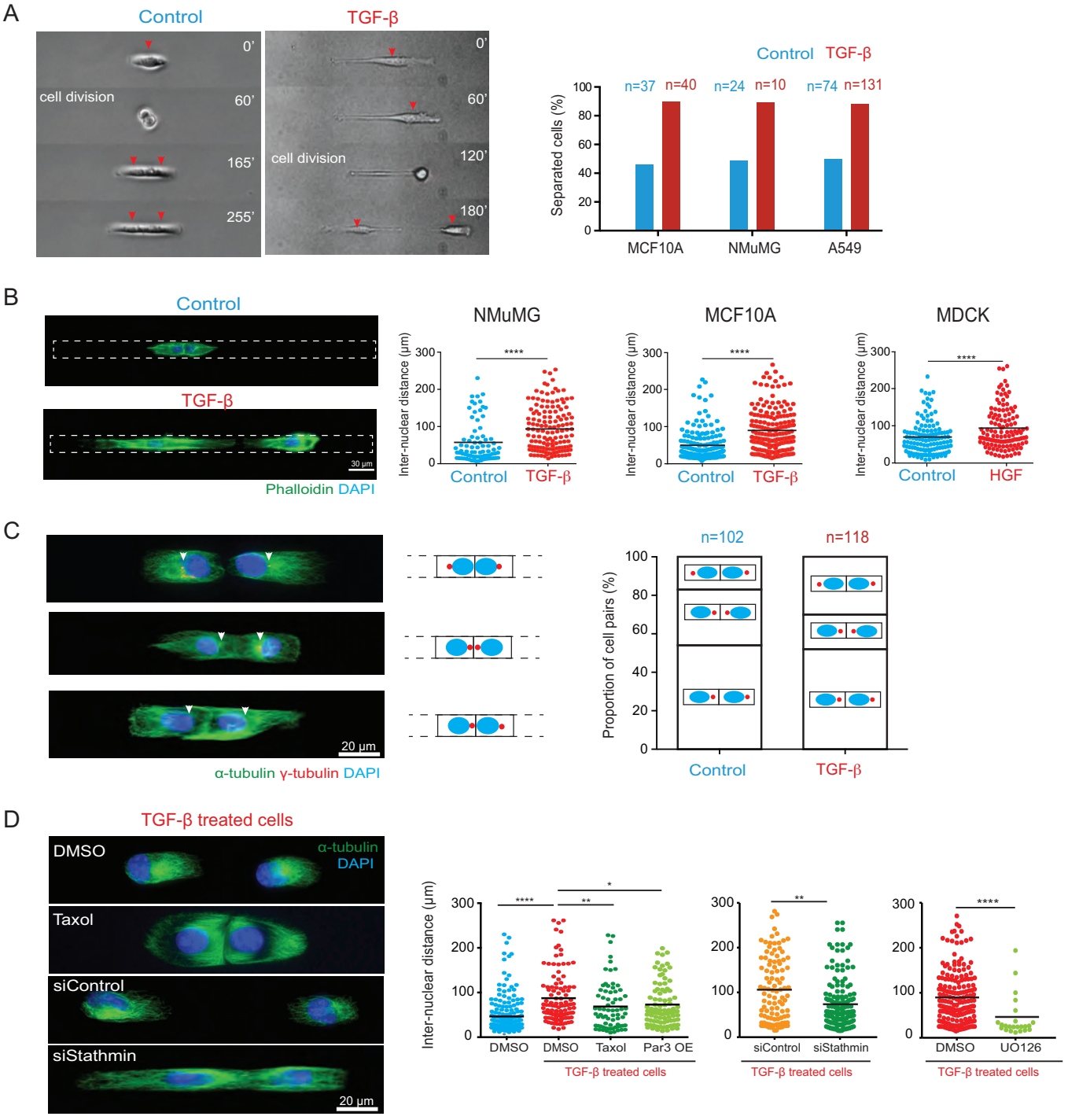
A
Control
TGF-β
cell division
0'
60'
165'
255'
cell division
0'
60'
120'
180'
Control TGF-β
n=37 n=40 n=24 n=10 n=74 n=131
Separated cells (%)
MCF10A
NMuMG
A549
B
Control
TGF-β
30 μm
Phalloidin DAPI
NMuMG
MCF10A
MDCK
Inter-nuclear distance (μm)
****
Control
TGF-β
HGF
C
20 μm
α-tubulin γ-tubulin DAPI
n=102
n=118
Proportion of cell pairs (%)
Control
TGF-β
D
TGF-β treated cells
DMSO
α-tubulin
DAPI
Taxol
siControl
siStathmin
20 μm
Inter-nuclear distance (μm)
DMSO
DMSO
Taxol
Par3 OE
TGF-β treated cells
siControl
siStathmin
DMSO
UO126

# Figure 7

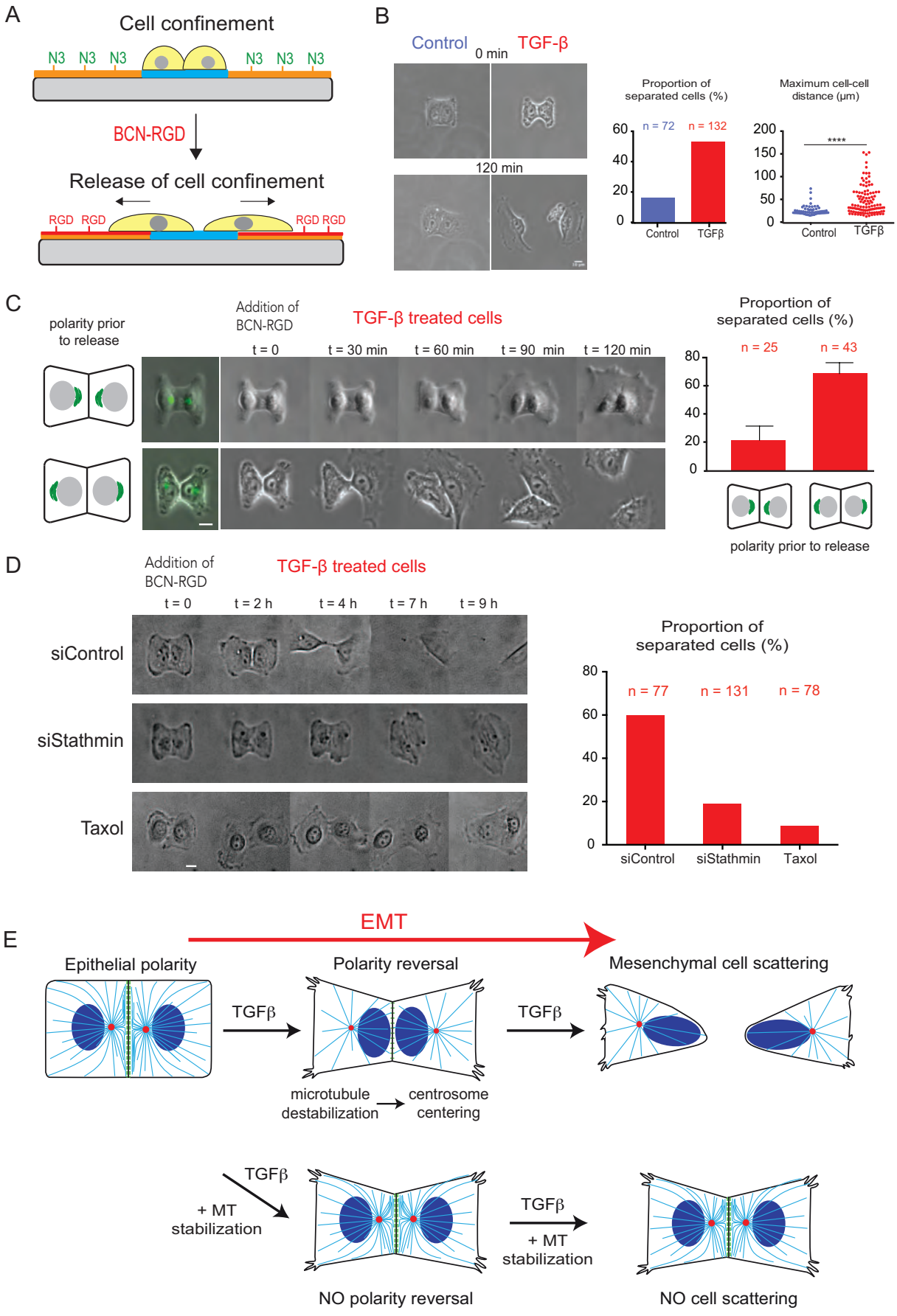
A
Cell confinement
N3 N3 N3 N3 N3 N3
BCN-RGD
Release of cell confinement
RGD RGD RGD RGD
B
Control
TGF-β
0 min
120 min
Proportion of separated cells (%)
n = 72
n = 132
Control
TGFβ
Maximum cell-cell distance (μm)
****
Control
TGFβ
C
polarity prior to release
Addition of BCN-RGD
TGF-β treated cells
t = 0
t = 30 min
t = 60 min
t = 90 min
t = 120 min
Proportion of separated cells (%)
n = 25
n = 43
polarity prior to release
D
Addition of BCN-RGD
TGF-β treated cells
t = 0
t = 2 h
t = 4 h
t = 7 h
t = 9 h
siControl
siStathmin
Taxol
Proportion of separated cells (%)
n = 77
n = 131
n = 78
siControl
siStathmin
Taxol
E
EMT
Epithelial polarity
Polarity reversal
Mesenchymal cell scattering
TGFβ
TGFβ
microtubule destabilization
centrosome centering
TGFβ
+ MT stabilization
TGFβ
+ MT stabilization
NO polarity reversal
NO cell scattering

# Polarity Reversal by Centrosome Repositioning Primes Cell Scattering during Epithelial to Mesenchymal Transition

Mithila Burute [1,2,3], Magali Prioux [2], Guillaume Blin [4], Sandrine Truchet [5], Gaëlle Letort [2], Qingzong Tseng [2], Thomas Bessy [1], Sally Lowell[4], Joanne Young[3], Odile Filhol-Cochet [6], Manuel Théry [1,2*]

[1] CytoMorpho Lab, A2T, UMRS1160, Institut Universitaire d'Hématologie, Hôpital Saint Louis, INSERM/AP-HP/Université Paris Diderot, 1 Avenue Claude Vellefaux, 75010 Paris, France.
[2] CytoMorpho Lab, LPCV, UMR5168, Biosciences & Biotechnology Institute of Grenoble, CEA/INRA/CNRS/Université Grenoble-Alpes, 17 rue des Martyrs, 38054 Grenoble, France.
[3] CYTOO SA, 7 Parvis Louis Néel, 38040 Grenoble, France.
[4] MRC Centre for Regenerative Medicine, Institute for Stem Cell Research, School of Biological Sciences, University of Edinburgh, 5 Little France Drive, EH16 4UU Edinburgh, United Kingdom.
[5] GABI, INRA/AgroParisTech/Université Paris-Saclay, Domaine de Vilvert, 78352 Jouy-en-Josas, France.
6 Laboratoire de Biologie du Cancer et de l'Infection, UMRS1036, Biosciences & Biotechnology Institute of Grenoble, CEA/INSERM/Université Grenoble-Alpes, 17 rue des Martyrs, 38054 Grenoble, France.

*Correspondence: manuel.thery@cea.fr

## Inventory of Supplementary Materials

Figure S1

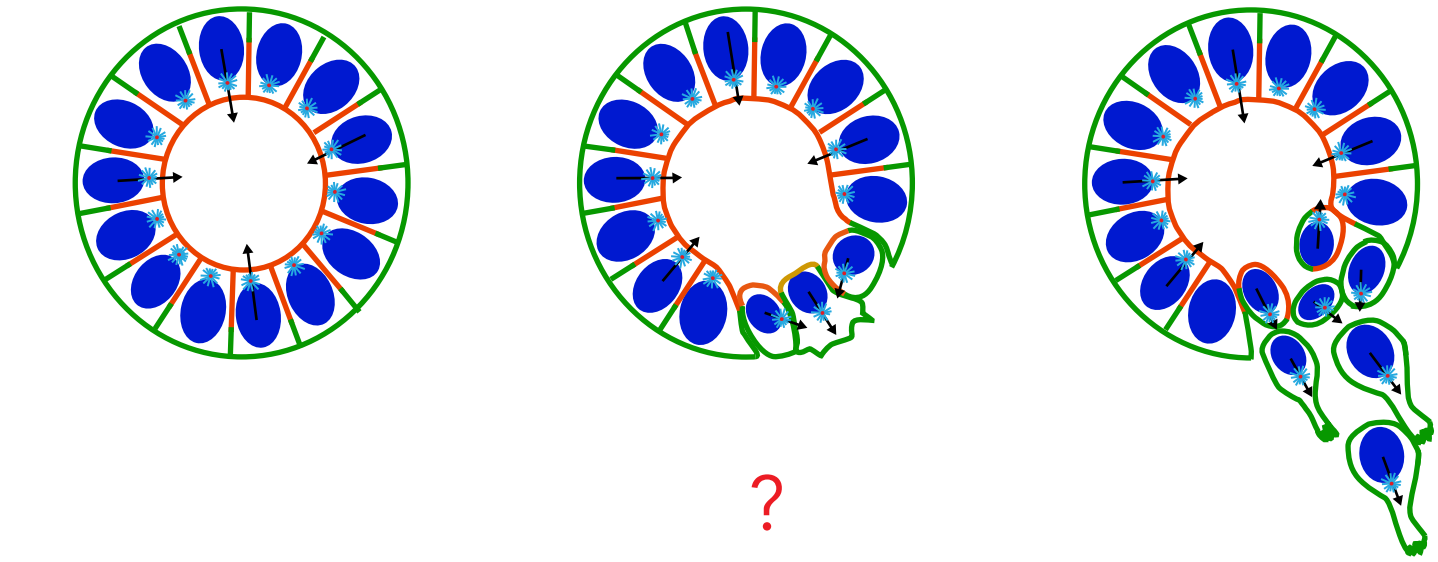
?
Apico-Basal Polarity
Polarity Reversal
Front-Rear Polarity

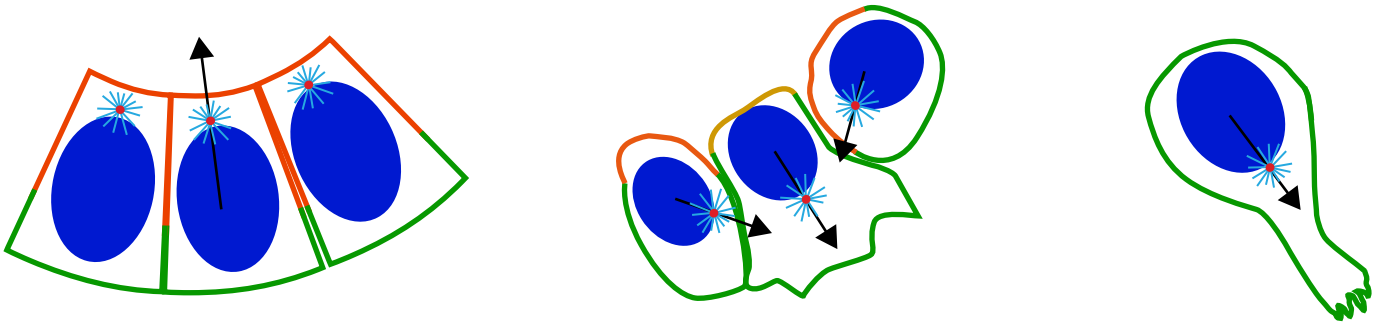

**Figure S1. Proposed model of polarity reversal during EMT progression, related to Figure 1 and Figure 2.**

Proposed model for driving changes from epithelial (apico-basal polarity) to single cell-mesenchymal (front-rear polarity) with inversion of internal polarity axis, which is defined by nucleus-centrosome vector. Intermediate states may involve polarity reversal of internal axis before cells separate from each other. Nuclei (blue), centrosome (red dot), basolateral (green) and apical membrane (red).

# Figure S2

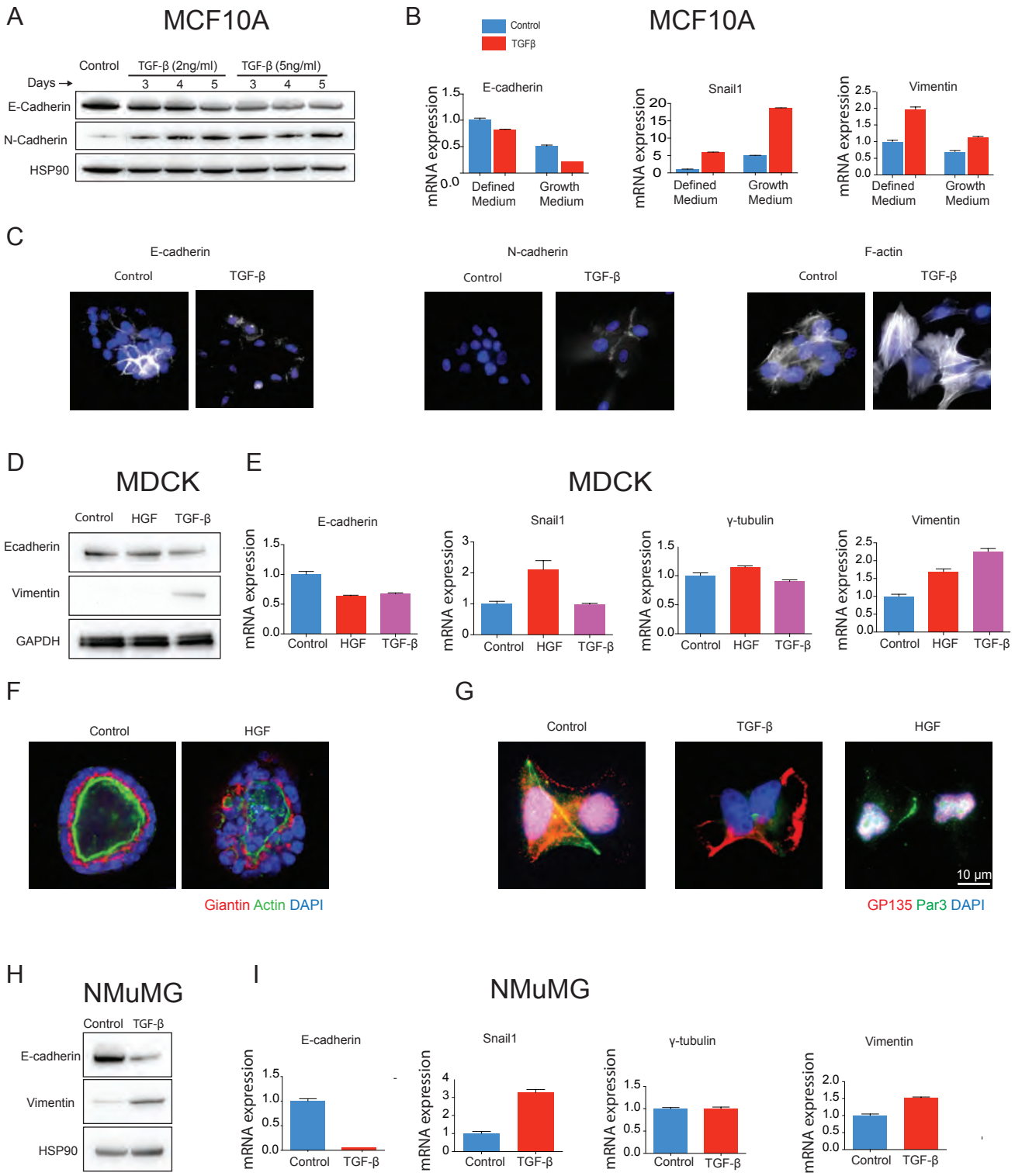
A
MCF10A
Control
TGF-β (2ng/ml)
TGF-β (5ng/ml)
Days →
3 4 5 3 4 5
E-Cadherin
N-Cadherin
HSP90
B
MCF10A
Control
TGFβ
E-cadherin
Snail1
Vimentin
mRNA expression
Defined Medium
Growth Medium
C
E-cadherin
N-cadherin
F-actin
Control
TGF-β
D
MDCK
Control HGF TGF-β
Ecadherin
Vimentin
GAPDH
E
MDCK
E-cadherin
Snail1
γ-tubulin
Vimentin
mRNA expression
Control HGF TGF-β
F
Control
HGF
Giantin Actin DAPI
G
Control
TGF-β
HGF
10 μm
GP135 Par3 DAPI
H
NMuMG
Control TGF-β
E-cadherin
Vimentin
HSP90
I
NMuMG
E-cadherin
Snail1
γ-tubulin
Vimentin
mRNA expression
Control TGF-β

**Figure S2. Molecular characterization of EMT induction in MCF10A, MDCK and NMuMG, related to Figure 2**

(A) Western blot of MCF10A cell lysate probed for E-cadherin, N-cadherin and loading control, HSP90 at different concentrations of TGF-β treatment over 3-5 days.

(B) Quantitative-PCR to analyze mRNA expression of E-cadherin, Snail1 and vimentin for cells cultured in defined medium and serum supplemented growth medium.

(C) Images of MCF10A cells stained for E-cadherin, N-cadherin and F-actin before and after TGF-β treatment.

(D) Western blot of MDCK cell lysate probed for E-cadherin, vimentin and GAPDH loading control.

(E) Quantitative-PCR to analyze mRNA expression of E-cadherin, Snail1, γ-tubulin, vimentin using U6 as control mRNA of MDCK cells.

(F) Images of MDCK acini stained for Golgi apparatus (red), F-actin (green) and nuclei (blue) in control and HGF treated cells.

(G) Images of MDCK cells on H-micropattern labeled for Par3 (green), GP135(red) and nuclei (blue).

(H) Western blot of NMuMG cells probed for E-cadherin, vimentin and loading control HSP90.

(I) Quantitative-PCR to analyze mRNA expression of E-cadherin, Snail1, γ-tubulin, vimentin using U6 as a control mRNA of NMuMG cells.

# Figure S3

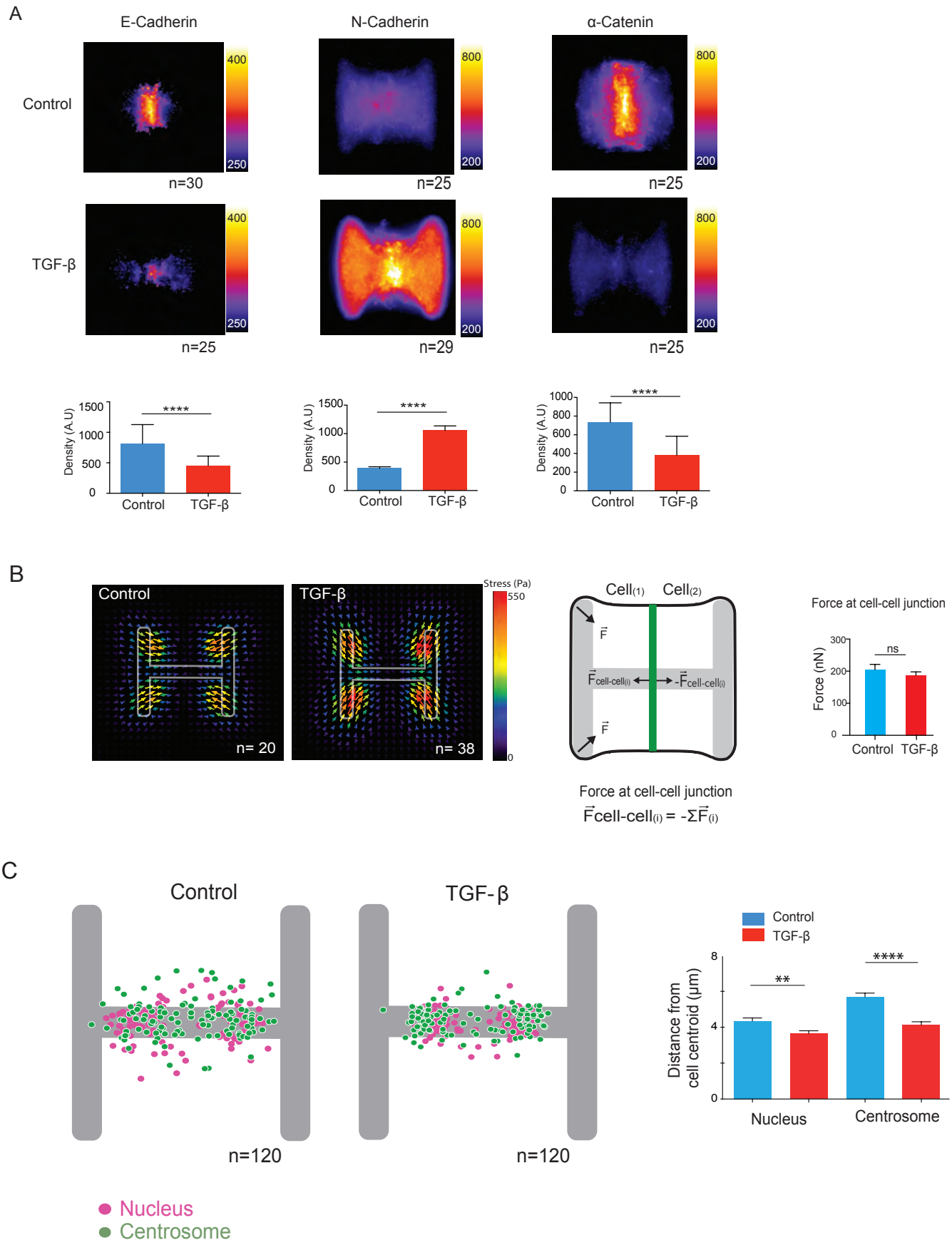
A
E-Cadherin
N-Cadherin
α-Catenin
Control
TGF-β
400
250
800
200
n=30
n=25
n=25
n=25
n=29
n=25
Density (A.U)
1500
1000
500
0
****
Control
TGF-β
1000
800
600
400
200
B
Control
TGF-β
n= 20
n= 38
Stress (Pa)
550
0
Cell(1)
Cell(2)
Force at cell-cell junction
Force (nN)
300
200
100
ns
Force at cell-cell junction
Fcell-cell(i) = -ΣF(i)
C
Control
TGF-β
n=120
n=120
Nucleus
Centrosome
Distance from cell centroid (μm)
8
4
0
**
****

**Figure S3. Changes in cell-cell junction after EMT, related to Figure 2.**

(A) Average images of MCF10A cell doublets labeled form E-cadherin, N-cadherin and α-Catenin. Scale bars on the right indicate intensity units. Intensities are quantified below.

(B) Average force fields (in Pascal) are obtained from traction force microscopy data. Force sustained at cell-cell junction (Fcell-cell) is calculated by a model used previously (Maruthamuthu et al., 2011).

(C) Quantification of the nucleus and centrosome distance to the cell centroid.

**Table S1: Main parameters used in simulations using Cytosim software**

| Name | Value | Description |
|---|---|---|
| **General** | | |
| Cell confinement | 18 * 10 $\mu m^2$ | Rectangular space |
| Cell viscosity | 1 $pN.s.\mu m^{-2}$ | (Kimura and Onami, 2010) |
| Simulated time | 400 s | |
| Time step | 0.05 s | Compromise exactitute / simulation time |
| Temperature | 25°C | Room temperature |
| **Centrosome** | | |
| Anchoring stiffness | 500 pN/µm | Stiffness of each MT minus_end anchoring to centrosmal complex |
| Radius | 0.5 µm | ~ centrosome radius |
| **Microtubules MT** | | |
| MT segmentation | 0.5 µm | Compromise exactitude / simulation time |
| MT persistence length | 5200 µm | (Gittes et al., 1993) |
| Polymerization force | 5 pN | (Dogterom, 1997) |
| Polymerisation (resp. shrinking) speed | 0.13 (resp. -0.27) $\mu m.s^{-1}$ | (Burakov, 2003) |
| Rescue rate | 0.064 $s^{-1}$ | (Burakov, 2003) |
| Catastrophe rate | 0.01, 0.04 $s^{-1}$ | Free and stalled catastrophe rate, Janson 2003 |
| Initial MT length | 0.75 µm (+-0.05) | Initial length distribution of Mts around centrosome (mean and standard deviation) |
| **Dyneins** | | |
| Dynein stall force | 1.1 pN | (Soppina et al., 2009), (Gross et al., 2000) |
| Dynein max speed | 1.5 µm/s | (Soppina et al., 2009), (Gross et al., 2000) |
| Dynein stiffness | 10 pN/µm | Strength of dynein anchoring to their cytoplasmic position |
| Binding rate | 5 $s^{-1}$ | Binding rate of a free dynein within binding range of MT |
| Binding range | 0.1 µm | Distance to MT from which dynein can bind it |
| Unbinding rate | 0.05 $s^{-1}$ | Unbinding rate of bound dynein |
| Unbinding force | 2 pN | Opposite force that will make dynein unbind MT |
| Dynein density | ~1.5 dyn/$\mu m^2$ | Estimated in (Zhu et al., 2010) |

**Movie Legend**

**Movie S1**. 3D reconstruction of two TEBs showing cells in front of the TEB with nucleus-golgi axis facing away from the central lumen. Cells with reverse polarity are marked with arrows.

**Movie S2**. Cytosim simulation showing 100 microtubules (top) and 250 microtubules (bottom) emanating from MTOC (yellow) and effect of their interaction with cell border and cytoplasmic dynein (green) on centrosome trajectory and final position.

**Movie S3**. Movie showing control (top) and TGF-β treated (bottom) NMuMG cells migrating on line micropatterns of 10 μm thickness.

**Movie S4**. TGF-β treated MCF10A cells with nucleus-centrosome axis toward cell-cell junction (left) and toward cell-matrix adhesion (right) are released from confinement by addition of BCN-RGD

**Movie S5.** Control siRNA (left), Stathmin siRNA (middle) transfected and Taxol treated TGF-β transformed (right) MCF10A cells are released from confinement by addition of BCN-RGD.

# Supplemental Experimental Procedures

**Cell Culture and EMT Induction**

Michigan Cancer foundation (MCF10A) human mammary gland cells (ATCC #CRL-10317) were maintained at 37°C at 5% $CO_2$ in Lonza Mammary Epithelial Growth Medium (Lonza MEGM bullet kit #CC3150 without Gentamycin) in the presence of 100 ng/ml of cholera toxin (Sigma #C-8052) and 0.5% antibiotic-antimycotic (Life Technologies #15240062). Cells were harvested by TrypLE™ (Life technologies #12605036) treatment for 12 min. An equal volume of soybean defined trypsin inhibitor (Life Technologies #R007100) was added followed by centrifugation at 200xg for 4 min. Cells were subcultivated in ratio less than 1:5 to maintain a stable epithelial phenotype. Medium was renewed every 2-3 days. 8000 cells/$cm^2$ were treated with 5 ng/ml TGF-β1 (R&D systems #240-B-002) in complete medium containing DMEM/F12 (Life Technologies #31331093), 5% horse serum (Gibco #16050-122), 25 ng/ml EGF (Peprotech TEBU #100-15), 100 ng/ml of cholera toxin, 10 μg/ml insulin (Sigma #I-1882), 500 ng/ml hydrocortisone (Sigma #H-0888), 0.5% antibiotic-antimycotic. For EMT induction, cells were treated TGF-β (5ng/ml) for 3 days then were passaged and cultured for another 2 days in the presence of TGF-β. Madin Darby Canine Kidney (MDCK) cells were maintained in DMEM-High glucose (Life Technologies #31966047) containing 10% fetal bovine serum (Invitrogen). EMT was induced by addition of 10ng/ml Hepatocyte Growth factor (Gibco #PHGO254) or 5ng/ml TGF-β for 3 days. EpH4 cells (Clone J3B1A) were a gift from Priscilla Soulie. Cells were maintained in DMEM containing 10% decomplemented Donor Bovine Serum (Gibco #16030-074). NMuMG cells (ATCC #CRL-1636) were cultured in DMEM containing 10% decomplemented fetal bovine serum and 10 μg/ml of insulin. EMT was induced in both cell lines by addition of TGF-β to the medium at 2 ng/ml for up to 3 days.

**3D Acini Culture and Immunofluorescence Microscopy**

Tip boxes, pipettes, eppendorf tubes, culture plates were pre-chilled at 4°C before the start of the experiment to prevent Matrigel polymerization. 50 μl of Matrigel (Sigma #E1270) was spread at the bottom of chamber slides-8 well (VWR #734-0088). MCF10A cells were trypsinized and resuspended in DMEM/F12 Glutamax medium (Life Technologies #31331093) supplemented with 2% horse serum, 500 ng/ml of hydrocortisone, 100 ng/ml of cholera toxin, 10 μg/ml of insulin, 5 ng/ml of EGF and 2% Matrigel. 4000 cells were seeded per well in 400 μl of medium. Medium was changed every 3 days. Seven-day MCF10A acini were transfected with 50nM of stathmin siRNA. Twenty-four hour after the transfection, 5ng/ml of TGF-β was added to the medium. Acini were fixed at Day 10. A similar procedure was performed for MDCK cells except

using Minimal Essential Medium (Gibco #11140035) supplemented with 4% fetal bovine serum and 2% Matrigel. Acini were cultured for 8-10 days and fixed in 2% PFA for 20 min at room temperature. Acini were permeabilized with 0.5% Triton X-100 in PBS for 10 min at 4°C followed by 3 washes with 100 mM Glycine in PBS (Wash solution). Cells were saturated with 0.1% BSA in the presence of 0.2% Triton X-100 and 0.05% Tween-20 in PBS (Saturation solution) for 1 h at RT. Acini were incubated with primary antibody diluted in Saturation solution for 3 h followed by 3 washes of 15 min each at room temperature. Secondary antibody was diluted in Saturation solution and acini were incubated in it for 2 h followed by 3 washes of Wash solution. Acini were mounted on a coverslip with Prolong gold antifade reagent (Molecular Probes #P36935).

**Mouse Mammary Gland Tissue and Immunofluorescence**

C3H mice were bred at INRA (UE0907 IERP, Jouy-en-Josas, France). Mice were euthanized by cervical dislocation at 6-7 weeks of age, and the inguinal mammary glands were immediately excised. All ethical aspects of animal care complied with the relevant guidelines and licensing requirements laid down by the French Ministry of Agriculture and the procedures used were approved by the local ethics committee (*Comethea* Jouy-en-Josas/AgroParisTech). Mammary fragments were rinsed in PBS and fixed with 4% PFA in PBS for 10-15 min at 4°C. Fixed tissues were infused for 16-24 h at 4°C in 40% sucrose in PBS, embedded in Tissue-Tek (VWR #25608-930), frozen in liquid nitrogen and stored at -80°C. Ten micrometer sections were rinsed with PBS at room temperature, permeabilized with 0.2% Triton-X100 in PBS and saturated with 3% bovine serum albumin (BSA) in PBS for 1 h. Incubation with the primary antibody (anti-giantin rabbit pAb, Abcam ab24586, 1:300 dilution) was allowed overnight at 4°C followed by four washes (10 min each) with PBS. Tissue sections were incubated with an Alexa Fluor 488-conjugated donkey anti-rabbit IgG (Molecular Probes #A-21206, 1:1000) secondary antibody for 1.5 h at room temperature and then washed with PBS as above. Actin was stained using Rhodamine Phalloidin (Molecular Probes #R415, 1:300 dilution in PBS) for 15 min at RT. Slides were mounted with Vectashield containing DAPI (Vector Laboratories #H-1200) and stored at 4°C until observation. Primary and secondary antibodies were all diluted in 2% BSA. Each experiment was performed at least twice and included control sections without primary antibody. Images were acquired with CSUX1-A1N Nikon Spinning Disk confocal microscope (Yokogawa) and EMCCD evolve 512 camera (Photometrics) using plan apochromat 40x, 1.3 NA oil objective.

**Mouse Embryo Whole Mount Immunofluorescence**

Wild type, outbred MF1 mice were maintained on a 12-h-light/12-h-dark cycle. For timed

matings, noon on the day of finding a vaginal plug was designated E0.5. Dissections of post-implantation embryos were performed as described in (Copp AJ et al., Prog Neurobiol. 1990). Post-implantation mammalian embryos were costained (overnight incubation of antibodies) for γ-Tubulin (Abcam #ab11316, 1:250), T-Brachyury (R&D #AF2085, 1:200), Collagen IV (Abcam #ab6586, 1:400) and counterstained with Dapi. Confocal microscopy was performed after dehydration through a PBS/methanol series (10 min each), three 5 min washes in 100% methanol, clearing in 1:1 v/v methanol/BA:BB (2:1 benzyl alcohol:benzyl benzoate), and two washes in BA:BB. Embryos were imaged directly in BA:BB using a Leica Sp8 confocal microscope and a 40X oil objective.

**3D analysis of Nucleus-centrosome vectors in whole embryo**

Image analysis of polarity within the embryo was performed with a custom built software (Blin G article in preparation), which includes automatic segmentation of nuclei, centrosome detection and embryonic cavity identification. Cells belonging to the epiblast were identified by filtering cells less than 15 um away from the outline of the cavity, T-Brachyury positive cells were defined as having an average Intensity of at least 500 (a.u). Cells from the ectoplacental cone were excluded by identifying a plane in the image, which would segregate the cone from the rest of the embryo.

**Micropattern Fabrication and Cell Seeding**

*Fabrication of micropatterns on glass*

A glass plate 10x10 cm (Schott #1304369) was cleaned using an air pistol and the surface of the glass plate was coated with adhesion promoter, TI Prime (Microchemicals) using a spin-coater (Laurell #WS-650m2-23NPPB) at 3000 rpm for 30s. The glass plate was baked at 120°C for 2 min on a hot plate. The glass plate was then coated with 1% solution of polystyrene (MW 260,000 Acros Organic # 178891000) in toluene (Sigma #179418) using a spin-coater at 1000 rpm. The polystyrene layer was further oxidized with an air plasma treatment (Plasma Etch #PE-30) for 20 s at 30W under vacuum at a 10 cc/min flow rate of air and incubated with Poly-l-Lysine-Polyethylenglycol (PLL(20)-g[3.5]-PEG(2) SurfaceSolutionS, Switzerland) in 10mM HEPES, pH 7.4 at room temperature for 30 min. PLL-PEG coated slides were placed in contact with an optical mask (Toppan Photomask) containing the transparent micropatterns using a vacuum chamber, then exposed to deep UV light using UVO cleaner (Model No. 342A-220, Jelight, USA) for 4 min

at power 6mW/cm2, λ 190nm at a distance of 1cm from the lamp. Micropatterned slides were subsequently incubated with a PBS solution containing 20 µg/mL fibronectin (Sigma #F1141) or laminin (Sigma #L2020) or collagen (Life Technologies, #A1048301) along with 20 µg/mL Alexa 647-fibrinogen (Gibco #F135200) for 30 min followed by 3 washes of PBS. Coverslips were dried and then rinsed in sterile PBS before cell seeding.

*Fabrication of micropatterns on PAA gel*

To achieve compliant substrates for cell attachment, micropatterns were prepared on a polyacrylamide gel attached to a glass coverslip. For a detailed protocol, refer to Mask method (Vignaud et al., 2014). Briefly, a photomask was plasma treated and coated with PLL-PEG using surface activation as explained above. The mask was exposed to UV light for 4 min. The fibronectin and fibrinogen mixture was prepared in sodium bicarbonate buffer, 100 mM, pH 8.3 and incubated on the mask for 30 min. The solution was allowed to flow by keeping the mask vertical. A mixture of acrylamide and bis-acrylamide was freshly prepared for desired rigidity (Tse and Engler, 2010) and was degassed for 30 min. TEMED at 0.1% of total volume and 10% APS at 1% total volume were added to the acrylamide solution. 25 µl of acrylamide was placed onto the photomask where protein was adsorbed. A silanized glass coverslip was placed gently to spread the drop and the gel was allowed to polymerize for 30 min. The coverslip was removed gently with a scalpel and was placed into PBS solution with micropatterns facing up.

*Dynamic micropatterning*

Azide-PLL-PEG was coated onto a coverslip in a similar manner as for PLL-PEG. Micropatterns were etched by UV irradiation. Cells were seeded onto the coverslip and allowed to form cell doublets after 16 h. Cells were released from confinement by addition of 100 µM BCN-RGD dissolved in 1x PBS. (van Dongen et al., 2013). Note that micropatterns were not coated with any ECM protein to facilitate cell movement onto the RGD-coated surface upon addition of BCN-RGD.

*Cell seeding*

Approximately 0.5 million cells were seeded onto micropatterned chips of 20x20 mm size and non-adhered cells were washed off after 30 min, which almost always resulted in single cell attachment per micropattern. Cells were allowed to divide over 24 h prior to fixation.

**Cell Scattering on Line Micropatterns and Video Microscopy**

For video microscopy, glass coverslips were patterned without the layer of polystyrene and then plated with 150,000 cells per 20x20 mm coverslip. Medium was changed once enough cells

were attached to the coverslip. Coverslips were mounted on Chamlide chambers (CM-s20-1). Cells were then recorded with a Nikon Eclipse Ti-E with 10x phase contrast objective in transmitted light and a 15 min interval was set between pictures. The number of cell separation events after a single cell division was then counted manually.

**Indirect Immunofluorescence**

Cells plated on glass coverslips were fixed with 4% paraformaldehyde (PFA) in Cytoskeleton buffer (10mM HEPES pH 6.1, 138 mM KCl, 3 mM MgCl2, 2 mM EGTA) containing 0.5% Triton-X100 for 20 min. Autofluorescence was quenched by treatment with 1 mg/ml sodium borohydrate in PBS for 7 min. Cells were fixed 0.1% Gluteraldehyde and 3% paraformaldehyde. Coverslips with cells were incubated in primary antibody diluted in 1.5% BSA containing 0.1% Tween-20 for 1h. After 2 washes of PBS, the coverslip was incubated with specific secondary antibodies (Alexa Fluor Conjugated, Thermo Fischer Scientific) diluted in 1.5% BSA containing 0.1% Tween-20 for 30 min in the dark. DNA was stained with DAPI (1:5000, Sigma #D9542) for 2 min in PBS. Coverslips were mounted with Mowiol 4-88 (Sigma #81381). Antibodies used included γ-tubulin (1:5000, abcam #ab11317), giantin (1:500 abcam #24586), α-tubulin (1:500, Sigma #T6557), Par-3 (Millipore 07-330), E-cadherin (1:500, BD Biosciences #610181), acetylated Tubulin (1:10000, sigma #T7451), N-Cadherin (1:500, BD Biosciences #610920), α-catenin (1:100, #ab49105) EB1 (1:200, BD Biosciences #610534).

**Chemical treatments**

Blebbistatin (Sigma #B0560) and Y-27632 (Selleckchem #S1049) were added onto cell doublets on micropatterns formed 16 h after seeding at 25μM and at 20μM respectively for 6 h. Smad pathway inhibitor SB431542 (Selleckchem #S1067) and U0126 (Selleckchem #S1102) was added to MCF10A cells along with TGF-β for 5 days. Taxol (Paclitaxel Sigma #T7191) was added to cells to 1.5 μM for 5 hours. DMSO was added to control sample at equivalent volume.

**Microscopy and Image Analysis**

Fixed and fluorescently labeled cells were imaged using an epi-fluorescence Olympus microscope (up-right BX61) with 100x NA 1.4 oil objective. Stacks of images spanning 12 μm z-distance were acquired using a piezo motor at the same illumination setting for control (CTR) and TGF-β treated sample. Image analysis for centrosome positioning was performed using a series of Macros in Image J. Briefly; z-projection of each color channel was obtained using 'maximum z-projection' plugin followed by merging the 4 channels to obtain a composite image. Using Pattern Alignment plugin (https://sites.google.com/site/qingzongtseng/template-

matching-ij-plugin) images were aligned with the reference micropattern image. Nuclei in DAPI channel were detected using image thresh-holding and object size criteria. Centrosomes were detected with similar thresh-holding and by using nuclei Region Of Interest (ROI) as spatial reference. Finally nucleus-centrosome vector was computed by subtracting co-ordinates of centrosome from nucleus co-ordinates and was normalized by the nucleus radius as indicated in Figure 2.

**EB1 Comet Quantification**

Z-projected images of EB1 comets were obtained as described above. Background subtraction was performed using a rolling ball radius of 50. For analyzing nucleation capacity of the centrosome, ROI of 1.5μm radius was drawn around the centrosome labeled by Ninein. EB1 comets were detected in the selected ROI by 'Find Maxima' Process.

**Microtubule Intensity Quantification**

Images of microtubules were acquired using CSUX1-A1N Nikon Spinning Disk microscope (Yokogawa) with 100X, 1.3 NA objective and Evolve 512 EMCCD camera (Photometrics). Z-projected images 'Maximum z intensity' of alpha-tubulin staining were obtained as described above. A ROI 46x46 μm was selected containing the cell pair on <H> micropatterns. Total intensity of the image was measured in Image J for each image to quantify total microtubule density in each cell-pair. To quantify microtubule density at the cell-cell junction, a ROI of 3.2 μm thickness was drawn along the cell-cell junction and intensity of alpha-tubulin staining was measured.

**Generating Averaged Images**

Images of E-cadherin, N-cadherin, β-catenin and α-catenin, actin, phospho-myosin II and paxillin were averaged using Z project. Cell-doublets on H-shaped micropatterns were stained for junction proteins and images were aligned using 'Pattern Alignment plugin' with reference to the micropattern. Average intensity at each pixel of the image was calculated using the 'average intensity' projection type in Image J.

**Three-dimensional Acini Quantification**

Images of acini were acquired on a Nikon Spinning Disk microscope at 60x oil objective with a z-step of 500 nm. To determine angle alpha formed between normal to cell periphery and the nucleus-centrosome vector (Figure 1), 4-5 central planes of acini images were selected to obtain single layers of cells at the center of the acini. A normalizing line was drawn to the basal surface of cells, which was marked by phalloidin staining. Using the 'angle' measurement in Image J, the

value of alpha (0-180°) was determined providing the angle formed by vectors in the same plane. Only the central plane of acini was considered for these measurements in order to have a planar distance of cells to the center of the acini.

**Traction Force Microscopy**

*Passivation of beads with poly-ethylene-glycol (PEG)*

Fluorescent beads were PEG passivated to avoid cell attachment and intake of the beads by cells. Carboxylated polystyrene beads, 200 nm, dark red (660/680), 2% solids (Molecular Probes #F-8807) were diluted to 1:4 in 10 mM MES buffer pH 5.5 containing 8 mg/ml of N-hydroxysuccinimide (NHS) (Sigma #1130672) and 4 mg/ml 1-ethyl-3-[3-dimethylaminopropyl]carbodiimide hydrochloride (EDC) (Molecular Probes #E-2247). This solution was mixed with 4 mg/ml PLL-PEG prepared in 10 mM HEPES buffer pH8.5. The mixture was incubated on a rotator for 2 h at RT. The beads were finally spun down and resuspended in 10 mM HEPES buffer, pH 7.4 in 2x the original bead volume. NHS and EDC solutions were prepared freshly and the mixing step with PLL-PEG was performed within 30 sec to avoid formation of bead aggregates. PEG passivated beads were stored at 4°C over 1-2 months and before every use beads were sonicated for 5 min to remove small aggregates.

*Silanization of coverslips*

20x20mm glass coverslips were plasma cleaned for 3 min, 30W, 10 cc/min gas level with plasma cleaner (Plasma Etch #PE-30). Coverslips were treated for 10 min in solution containing 2% 3-triethoxymethylsilance (Sigma #339633) and 1% (v/v) acetic acid in ethanol. Coverslips were rinsed with ethanol and dried with air-gun followed by baking at 120°C for 1 h.

*Fabrication of micropatterns on PAA with fluorescent beads*

10 kPa polyacrylamide gels were prepared using 5% acrylamide and 0.3% bis-acrylamide solution. The solution was degassed for 15 min in a vacuum bell. Quartz mask (Toppan) was washed with soap followed by milliQ water and dried using nitrogen gas flow. The surface of the quartz mask was activated by plasma treatment at 100W for 3 min in air plasma cleaner. A drop of PLL-PEG solution (0.1 mg/ml, 10 mM, pH 7.4) was added onto the chromium side of the mask at the region of interest (ROI) and was covered with a clean 20x20 mm glass coverslip. After 30 min of incubation at RT, the mask was tilted to let the coverslip flow off with excess solution and the mask was allowed to dry by dewetting. The mask was UV insulated with the chromium side facing the UV lamp (UVO cleaner Model No. 342A-220, Jelight, USA) for 4 min at power 6mW/cm2, λ 190nm at a distance of 1cm from the lamp. The ROI on the mask was coated with 20 µg/ml of fibronectin (Sigma #F1141) and fibrinogen Alexa Fluor 647 (Molecular Probes

#F135200) dissolved in 100 mM of sodium bicarbonate buffer, pH 8.3 and was incubated for 30 min at RT. At the end of the incubation, excess solution was allowed to flow off the mask, which was then gently rinsed once with sodium bicarbonate buffer. PEG passivated polystyrene beads were sonicated in a water bath for 5 min and immediately added to Acrylamide-bis-acrylamide solution to 1:16 dilution (0.06% solid beads) and mixed well with the help of a pipette. Once the mask was dried, 25 µl of Acrylamide and Bis-acrylamide solution was put onto the ROI on the mask and was immediately covered with a silanized glass coverslip while making sure there was no bubble introduced in the gel. After 25 min of polymerization, the polyacrylmide gel with coverslip was flooded with sodium bicarbonate buffer to facilitate detachment of the gel. The gel was detached gently from the mask using a sharp scalpel. The silanized coverslip containing polymerized gels with micropatterns was stored at 4°C in PBS solution with micropatterns facing up until further use.

Cells were seeded onto micropatterns on PAA as described for glass substrates. A glass coverslip with PAA gel and cells was mounted in a magnetic chamber (Live Cell Instrument, Chamlide CMS). Images of fluorescent beads (136x136 $um^2$) were acquired at 63X, 1.4 NA Plan Apochromat VC (Nikon) on CSUX1-A1N Nikon Spinning Disk microscope (Yokogawa) and Evolve 512 EMCCD camera (Photometrics). Stacks of five images with 0.5 µm z-distance were acquired around the topmost focused beads plane. Cells were trypsinized at 37°C in the chamlide chamber with extreme care so as to not move the chamber on the microscope. Cells were washed away with the help of the pipette after 10 min. Images of the beads were acquired at the positions registered before.

*Calculations of cellular forces*

Image analysis macros and plugins and tutorial for Image J for traction force microscopy analysis can be found at (https://sites.google.com/site/qingzongtseng/piv). Briefly, the best-focused and top-most plane of bead images of before and after trypsinzation of cells was selected. Images of beads from independent cell doublets were aligned using normalized cross-correlation algorithm of the plugin-'Align slices in stack' and with the micropattern as a reference. The Displacement field was computed from bead movements using iterative Particle Image velocimetry (PIV) algorithm. Parameters used for Iterative PIV were 3 interrogation window 204, 25, 12 pixel and correlation 0.6. Traction forces were calculated from displacement field using Fourier Transform Traction Cytometry (FTTC) algorithm. Parameters used for FTTC were, Young's Modulus 10000 Pa, Regularization factor of 10^-9, Poisson ratio 0.5. The stress field values were obtained in Pascal units. The product of unit grid area (3.2x3.2 µm) and the traction stress vector generated the traction force vector (nN).

Force vectors at each position were averaged over several images to obtain averaged force fields for cell-pairs. Cell-cell force (Fcell-cell) was computed by from the vector sum of traction forces for each cell on H-micropatterns and negative imbalanced force was designated as Fcell-cell.

**Transient Cell Transfection**

250,000 MCF10A cells were seeded in a single 6 well plate. Par3 siRNA was added to the defined MEGM medium to 10 nM along with RNAiMax reagent (Invitrogen #13778030). After 24 h, cells were seeded onto micropatterns and were allowed to divide for another 24 h before fixation. On-Target plus SMART pool was used for Par3 siRNA (Dharmacon L-015602-00-0005) J-015602-05, AAGCAUGGAUUUAGGUAUA, J-015602-06 AGACUAAACUCAAUACAGU, J-015602-07 CGAUAAAGACAGACUGGUA, J-015602-08 GAUGGCGACCUUCGAAAUA. Control siRNA (Qiagen #SI03650318) was used at 20 nM. Cells were transfected with 20nM of Stathmin siRNA. Cells were seeded onto micropattern after 24 hours and TGF-β was added to cells. After 24 hours cells were fixed. On-Target plus SMART pool was used for Stathmin siRNA (Dharmacon L-005152-00-0005) J-005152-07 GAAAGACGCAAGUCCCAUG, J-005152-08 UAAAGAGAACCGAGAGGCA, J-005152-09 GAAACGAGAGCACGAGAAA, J-005152-10 GAAGAGAAACUGACCCACA. MCF10A cells were transfected with pk-myc-Par3b construct (Addgene #19388) using Plus Reagent (Invitrogen #11514015) according to manufacturer instructions. Twenty-four hour after transfection cells were treated with TGF-β and seeded onto micropatterns 24 h after. Following one cell division, cells on micropatterns were fixed. Cells used for dynamic micropatterning were seeded at a density of 125,000 the previous day followed by addition of 2 µl of CellLight Golgi-GFP BacMam 2.0 (Molecular Probes #C10592) per 10,000 cells. Cells were imaged after 30-48 h of incubation.

**Quantitative PCR**

qRT-PCR was used to analyze mRNA expression levels of E-cadherin, snail1, vimentin and γ-Tubulin. RNA was extracted in TRIzol (Ambion 15596-026) and chloroform extraction. RNA quantity was measured using Nanodrop2000. cDNA was synthesized using Affinity script qPCR synthesis kit (Stratagene #600559). The reagents used were SYBR® Green PCR Master Mix and SYBR® Green RT-PCR Reagents Kit (CFX96 Touch™ Real-Time PCR Detection System from BioRad).

Primers for MDCK cells (Dog origin)

E-Cadherin F: 5′-TGACAGCTACACGTTCACCG-3′ R: 5′-TTCAAAACTCACCCTGCCCA-3

Snail1 F 5′-AAGATGCACATCCGAAGCCA-3′ R 5′-CTTCTCACCGGTGTGGGTC-3,

Vimentin F 5′-AAATGGCTCGTCACCTTCGG-3′ Vimentin R 5′-GAGCAATCCTGCTCTCCTCG-3′,
U6 F 5′GCAAGATGGCGGACAAAGAG-3′ U6 R 5′-TCGAACCCCTTCAAGATGCC-3′
g-Tubulin F 5′-CCGGTACCTGAGGAGCGAT-3′ R 5′-TTCCAGAACTCGAACCCAATCTG-3′

Primers used for NmuMG (Mouse)
Vimentin F 5′-TGCACGATGAAGAGATCCAGG -3′ , R 5′-AGGCTTGGAAACGTCCACAT -3′
g-Tubulin forward 5′-GGAGCGATGCCGAGAGAAAT-3′R 5′-CCAGAACTCGAACCCAATCTGA -3′
Snail1 5′-TGTGTGGAGTTCACCTTCCAG-3′ Snail1 R 5′-AGAGAGTCCCAGATGAGGGT -3′
g-Tubulin forward 5′-GGAGCGATGCCGAGAGAAAT-3′
g-Tubulin-reverse 5′-CCAGAACTCGAACCCAATCTGA -3′
E-Cadherin F 5′-GAAGGCTTGAGCACAACAGC -3′, R 5′-CCCTGATACGTGCTTGGGTT -3′
U6 F 5′-TGTGCTGTTGACGAGGACTT-3′, R 5′-GTTCCACAGATGCTCAGGTCA-3′

Primer used for MCF10A (Human origin)
E-Cadherin F 5′-CCCACCACGTACAAGGGTC-3′ R 5′-CTGGGGTATTGGGGGCATC-3′
Snail1 F 5′-AGGCAGCTATTTCAGCCTCCTGTT R 5′=TGACAGCCATTACTCACAGTCCCT-3′
Vimentin F 5′-AGAACCTGCAGGAGGCAGAAGAAT,R 5′-TTC CAT TTC ACG CAT CTG GCG TTC-3′
U6 F 5′-CTCGCTTCGGCAGCAGA-3′, R 5′-AACGCTTCAGGAATTTGCGT-3

**Western Blot**

For immunoblot analyses of proteins, cell lysates were prepared in RIPA lysis buffer (10 mM Tris-HCl [pH 7.4], 150 mM NaCl, 1% (v/v) Triton X-100, 0.1% (v/v) SDS, 0.5% (v/v) DOC and 1 mM EDTA) containing a protease inhibitor cocktail (Sigma P8340), phosphatase inhibitor cocktails 1 and 2 (Sigma-Aldrich P2850, P5726), and were cleared by centrifugation. Equivalent amounts of protein were processed to SDS-PAGE electrophoresis and transferred to nitrocellulose or PVDF membrane (Hybond-P, Amersham Biosciences). Immunoblotting was performed using the primary antibodies (anti-E-cadherin, anti-N-cadherin from BD Biosciences Pont de Claix, France; anti-HSP90 (Cell Signalling), anti-vimentin (clone Vim13.2) was from Sigma-Aldrich (Lyon, France), anti-GAPDH from (Invitrogen). The blocked membranes were incubated overnight with primary antibodies, washed with TBST and incubated with secondary antibodies conjugated to horseradish peroxidase. Detection was achieved by using Enhanced chemiluminescence method (ECL Plus, GE Healthcare).

**Numerical Simulations using Cytosim Software**

Simulations were performed using the Cytosim software (www.cytosim.org). Microtubules are considered as elastic fibers surrounded by a viscous fluid following Langevin dynamics (Nedelec and Foethke, 2007). We simulated only microtubules nucleated from and anchored to a centrosomal complex. New nucleation of microtubules, microtubules unbinding from centrosome or steric interactions between microtubules are not taken into account. Microtubules can grow at a force-dependent speed (Dogterom, 1997), can undergo catastrophe events and shrink, and can undergo rescue events. Their bending elasticity is modelled following Euler's buckling description. Microtubules are initially uniformly distributed around the centrosome and can freely rotate around it. They are constrained into a rectangular space with an Hookean rappel force and will push against this border but can glide freely along it. Cytoplasmic dyneins are modeled as immobile objects spread into the cellular space that can bind/unbind microtubules and move toward the MT minus end when bound, thus generating a pulling force on the centrosome.

**Statistical Analysis**

Mann-Whitney non-parametric test was used to compare differences between the samples. Error bars indicate standard error mean (SEM). N indicates numbers of experiments while n indicates sample size.

# Supplemental References


Azioune, A., Carpi, N., Tseng, Q., Théry, M., and Piel, M. (2010). Protein Micropatterns. A Direct Printing Protocol Using Deep UVs. Methods Cell Biol. *97*, 133–146.

Burakov, a. (2003). Centrosome positioning in interphase cells. J. Cell Biol. *162*, 963–969.

Copp. AJ., Brook FA., Estibeiro JP., Shum AS., Cockroft DL. (1990). The embryonic development of mammalain neural tube defects. Prog. Neurobiolo. 35(5):363-403

Dogterom, M. (1997). Measurement of the Force-Velocity Relation for Growing Microtubules. Science (80-. ). *278*, 856–860.

Gittes, F., Mickey, B., Nettleton, J., and Howard, J. (1993). Flexural rigidity of microtubules and actin filaments measured from thermal fluctuations in shape. J. Cell Biol. *120*, 923–934

Gross, S.P., Welte, M.A., Block, S.M., and Wieschaus, E.F. (2000). Dynein-mediated Cargo Transport In Vivo: A Switch Controls Travel Distance. J. Cell Biol. *148*, 945–955.

Kimura, A., and Onami, S. (2010). Modeling Microtubule-Mediated Forces and Centrosome Positioning in Caenorhabditis elegans Embryos. Methods Cell Biol. *97*, 437–453.

Maruthamuthu, V., Sabass, B., Schwarz, U.S., and Gardel, M.L. (2011). Cell-ECM traction force modulates endogenous tension at cell-cell contacts. Proc. Natl. Acad. Sci. U. S. A. *108*, 4708–4713.

Soppina, V., Rai, A.K., Ramaiya, A.J., Barak, P., and Mallik, R. (2009). Tug-of-war between dissimilar teams of microtubule motors regulates transport and fission of endosomes. Proc. Natl. Acad. Sci. U. S. A. *106*, 19381–19386.

Tse, J.R., and Engler, A.J. (2010). Preparation of hydrogel substrates with tunable mechanical properties. Curr. Protoc. Cell Biol. 1–16.

Zhu, J., Burakov, A., Rodionov, V., and Mogilner, A. (2010). Finding the Cell Center by a Balance of Dynein and Myosin Pulling and Microtubule Pushing : A Computational Study. *21*, 4418–4427.